Chapter 3

Stimulated Raman scattering: Ensembles to single molecules

Richard C. Prince and Eric O. Potma
University of California, Irvine, CA, United States

3.1 The birth and evolution of stimulated Raman scattering

Over the last few decades, the use of SRS as an analytical technique has grown rapidly and will continue to grow as more commercial turnkey systems enter the market. According to the *Clarivate Analytics* Web of Science, there are more than 6000 publications in the field of *stimulated Raman scattering* (SRS) and more than 70,000 articles citing work in that collection [1]. This is shown graphically in Fig. 3.1. In this section, we discuss the origin of the SRS approach, its coming of age as a sensitive molecular spectroscopy technique, and its growth into a popular label-free imaging technique.

Discovered shortly after the first demonstration of a working laser, the phenomenon of SRS has closely tracked that of the laser itself [2]. The pulsed action of some lasers, including Maiman's first ruby laser, creates extremely intense bursts of light, and it was quickly realized that these intense fields would enable the generation of various nonlinear phenomena [3]. The first prediction of a nonlinear optical effect had been worked out by Maria Göppert-Mayer in 1930 [4]. Remarkably, the demonstration of nonlinear optics occurred a year after the birth of the laser with Franken et al. demonstrating second-harmonic generation (SHG) and Kaiser demonstrating two-photon excitation [5, 6]. A year after these, in 1962, third-harmonic generation (THG) requiring even higher electric fields was demonstrated by Terhune [7]. In each of these cases, observation of a color different than that of the input light revealed the nonlinear process. The discovery of SRS would be no different.

The discovery of SRS was serendipitous. To achieve pulsed laser action, known then as a "giant ruby laser pulse," and thus the high peak intensity necessary to generate nonlinear effects, many labs turned to the use of Kerr-cell shutters to modulate the output of their lasers [8–13]. The common material for Kerr shutters of the time was nitrobenzene, a material with several strong Raman-active modes [14, 15]. In 1962, Woodbury and colleagues at the Hughes Research Laboratories reported in a brief correspondence anomalous laser lines from their ruby laser and identified that the lines depended on the operation of their nitrobenzene Kerr shutter [16]. An interpretation of the first Raman laser is shown in Fig. 3.2. An interesting historical note about this discovery was that it was made while conducting research on lasers for the US Air Force, and was reported in a now unclassified report [17].

These anomalous "satellite" lines of their pulsed reflector laser were correctly identified as a version of Raman scattering in research published later in 1962 [18]. In comparison to literature values, it was determined that the R-line of the ruby laser was shifted by an amount corresponding to the energy of the symmetric stretching mode of the NO_2 group of nitrobenzene, and subsequent measurements were made with different organic liquids to confirm Raman scattering as the origin of the effect. The authors made the realization that the amplification of the Raman lines was due to a similar process to that of the stimulated fluorescence emission that produces laser action. Thus, the name of SRS was stuck to this process.

By 1962, a theory of four-wave mixing to explain nonlinear light-matter interactions was already in place [19], and by the end of the decade, a semiclassical theory of SRS in terms of four-wave mixing was readily described [20, 21]. Explanations in the classical wave [21, 22] and quantized field regimes [23] were delineated, and it became possible to fully describe the SRS process in the laser cavity [24].

3.1.1 The birth of SRS: Light conversion and early spectroscopy

The first demonstrations of SRS were inherently spectroscopic in nature. The presence of a sufficient quantity of a Raman-active material produces additional laser lines at the Stokes and anti-Stokes frequency. In brief, the fundamental (pump)

Stimulated Raman Scattering Microscopy. https://doi.org/10.1016/B978-0-323-85158-9.00038-5

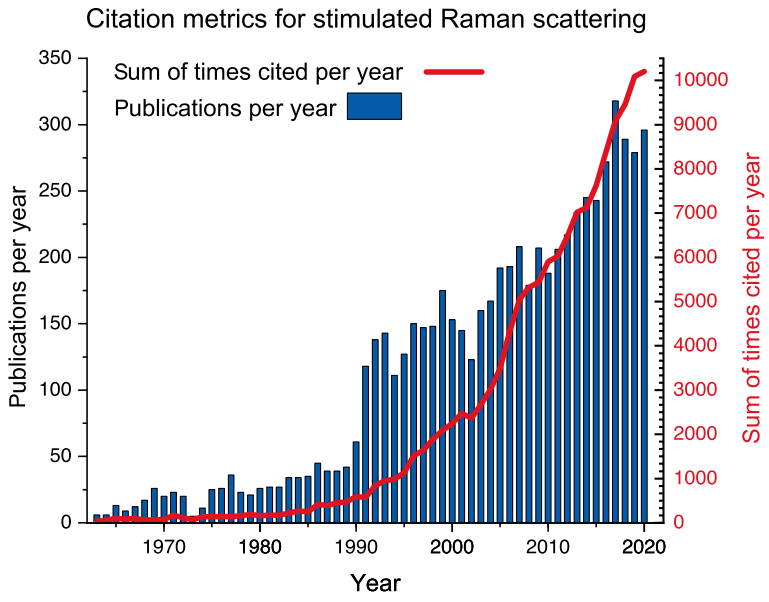

FIG. 3.1 The number of publications per year in the topic of stimulated Raman scattering and the sum of the total citations to articles mentioning stimulated Raman scattering per year. The academic product of stimulated Raman scattering has grown extensively since the discovery of the technique.

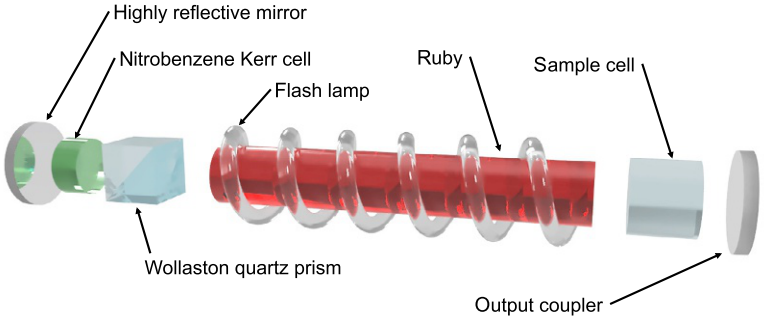

FIG. 3.2 Modern diagram of the original ruby laser Raman oscillator arrangement as used by Woodbury and Ng. *(Reproduced from a diagram in N. Bloembergen, The stimulated Raman effect, Am. J. Phys. 35 (11) (1967) 989–1023, https://doi.org/10.1119/1.1973774. Intense Stokes radiation is produced from the fluid in the sample cell and from the Raman-active mode of the nitrobenzene in the Kerr shutter.)*

laser line, ω_1 produces lower energy Stokes-shifted radiation through spontaneous Raman scattering, which involves Raman mode ω_v, producing radiation at $\omega_2 = \omega_1 - \omega_v$. The highly reflective cavity mirrors allow Stokes photons to travel the cavity and return to the Raman-active medium where they, in turn, stimulate the emission of more Stokes photons. Just as in stimulated fluorescence, this generates a coherent and highly directional beam at frequency ω_2. It is important to note that unlike normal stimulated emission no energy is stored in electronically excited states. Instead the difference in energy between the pump and Stokes photons is transferred to the Raman-active material in the form of excited vibrational modes at frequency ω_v. This follows the usual Raman relation: $\hbar\omega_v = \hbar(\omega_1 - \omega_2)$. Analogous to linear Raman scattering, stimulated anti-Stokes scattering is also observed wherein a beam blue shifted from the fundamental is produced, giving rise to radiation at $\omega_3 = \omega_1 + \omega_v$ [25–27].

Early on the use of SRS diverged into two distinct paths. The first path of research focused on the generation of coherent radiation, most widely in the form of Raman shifters. It was realized that SRS could be produced by placing the Raman-active material outside of the laser cavity, and in this way, external Raman-based shifters were achieved [28]. These first shifters used transparent crystals such as diamond and calcite, but use of other materials quickly became commonplace [29–31]. Of particular importance is the use of SRS to red-shift light in silica fibers by excitation of the Si–O modes around 13 THz (440 cm^{-1}) [32, 33]. SRS in fibers forms the basis of fiber Raman lasers and broadband Raman amplifiers [34, 35]. Both of these technologies have found major use in the fiber-based telecommunications industry [36, 37]. Research into Raman shifters and Raman lasers has continued several decades since their invention as a popular source of frequency conversion. The second path of research aimed to use SRS for studying the spectroscopic properties of materials, which are discussed next.

3.1.2 First wave: Picosecond time-resolved spectroscopy

Early on, many experts were skeptical about the utility of SRS as a spectroscopic tool. Bloembergen stated in a review from 1967 that "The spectroscopic information that may be obtained from the stimulated process is very restricted compared to the results from spontaneous scattering" [24]. Others realized the implication that coherent radiation implies coherent molecular motion. Early work focused on studying the dephasing dynamics of the Raman-active modes of various materials [38–40]. These lines of research were enabled by continually progressing research into lasers themselves as pulses into the picosecond became available [41, 42]. The short temporal pulse widths of these lasers were shorter than the dephasing times of Raman lines. As such, molecular vibrations could be coherently prepared in a material and the free induction decay of the excitation could be measured. Throughout the 1970s, SRS research followed the advances in picosecond laser technology. Many coherent Raman studies focused on the ground-state vibrations of materials in all three major physical states. The increasingly shorter pulse widths promised to allow SRS to disentangle the broadening mechanisms behind Raman line widths [43].

3.1.3 Second wave: Ultrafast and impulsive regimes

During the late 1970s and 1980s, SRS had a limited effect on the field of nonlinear optics and ultrafast spectroscopy. In many cases, it was experimentally easier to use the anti-Stokes signal at $2\omega_1 - \omega_2$ or the coherent Stokes signal at $2\omega_2 - \omega_1$. Coherent anti-Stokes Raman scattering (CARS) and coherent Stokes Raman scattering (CSRS), both third-order nonlinear techniques like SRS, overshadowed SRS during this time period.

The resurgence of SRS as a technique coincided with the invention of femtosecond laser sources, operating through various kinds of mode-locking mechanisms, including Kerr-lens mode locking [44–46]. This timeline of use is shown graphically in Fig. 3.3. Similar to stimulated Brillouin scattering, femtosecond pulses could be used to *impulsively* excite phonons in crystals [47, 48]. Due to the broad spectral profile of these pulses, both the ω_1 and ω_2 frequencies could be achieved in a single pulse and drive the phonon at the Raman frequency, $\omega_v = \omega_1 - \omega_2$ [49].

This new technique was given the name of impulsive stimulated Raman scattering (ISRS) as the temporal width of the pulses is shorter than the period of the vibrational modes under study. The study of crystalline solids was quickly expanded to include low-energy modes in liquids as well [50]. Low-energy modes, $<200\ \text{cm}^{-1}$, are typically hard to probe with CARS or CSRS because of the difficulty of spectrally filtering weak Raman-shifted contributions so close to the laser lines. Thus, SRS was able to fill a gap in the spectroscopist's repertoire allowing access to intra- and intermolecular vibrations and orientational modes of liquids as well as lattice dynamics in solids. Using ISRS, it was possible to resolve the evolution and dephasing of vibrational motion as a function of time [51]. More information about ISRS is found in Chapter 7.

The advent of ISRS led to a resurgence in the use of SRS for spectroscopy. While early experiments were conducted in optically transparent solids, ISRS was shown quite capable at studying electronically resonant molecules. With ISRS, the vibrational modes of excited states can be directly probed, thus offering a coherent view of electronic and vibrational coherences. As discussed elsewhere in this work, electronic resonances enhance the Raman response and boost signal yields. This

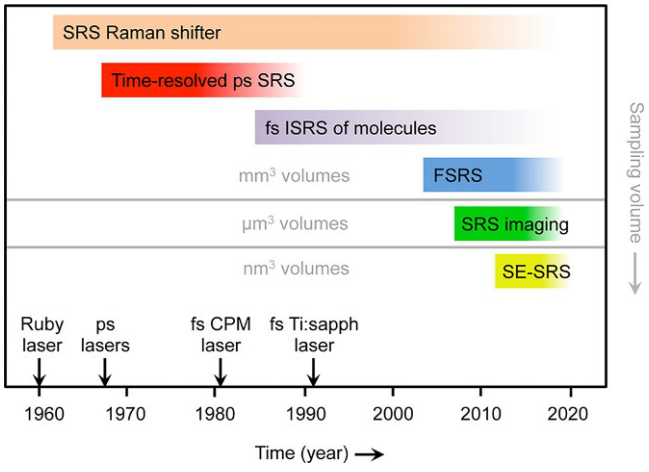

FIG. 3.3 Timeline of major developments in SRS technology.

allows for measurements at very low concentration of the chromophores, down to the μM range. This technique has been used extensively to study the vibrational dynamics of chromophores in solution [52–54].

Throughout the 1990s and into the early 2000s, the increasing versatility and availability of ultrashort Ti:sapphire lasers allowed for further advances in SRS techniques. In 2003, McCamant demonstrated what they called femtosecond stimulated Raman spectroscopy (FSRS), named for the time resolution of the measurement [55]. The FSRS was famously used to elucidate structural dynamics of biologically important molecules such as β-carotene and retinal [56]. Besides ISRS and FSRS, the family of vibrational spectroscopy methods that rely on a stimulated Raman transition also contains techniques such as the time-resolved optical Kerr effect (OKE) [57], used for studying low-energy Raman-active modes, and the Raman-induced Kerr effect (RIKES) [58], used for interrogating high-energy vibrational modes. Some of the principles of time-resolved SRS spectroscopy will be discussed in Section 3.2.

3.1.4 Third wave: Diffraction-limited microscopy

Maturation of the laser technologies in the late 20th century led to great increases in the sensitivity of SRS measurements. By combining these with various modulation techniques and lock-in-based detection, SRS measurements have been pushed to the point where the signal is limited only by laser shot noise, as discussed in Chapter 2. This directly translates into measurements of small volumes and lower concentrations.

Gains in sensitivity enabled the use of higher numerical aperture lenses and, eventually, microscopic imaging [59, 60]. Previous SRS techniques were performed in samples with an interaction distance on the order of several millimeters by focusing with a long focal length lens. With a high-NA lens, the focal length becomes on the order of a micrometer and the focal volume that of a femtoliter (fL). CARS was the first demonstration of a coherent Raman scattering process in a fL volume, performed in 1999 by Zumbusch [61]. CARS turned out to be the proving ground for coherent Raman microscopies, and is itself a widely used technique, as underlined by the release of commercial CARS microscopes [62–65].

Converting SRS for the purpose of microscopy proved to be a more difficult task than that of CARS. Unlike a spectroscopy experiment where the larger volumes would permit spatial separation of the input beams, high-NA conditions utilize a collinear excitation. An early implementation of the SRS principle with collinear excitation in an optical microscope came in 2001 in the form of optical Kerr effect spectroscopy. In this implementation of ISRS, low-energy librational Raman modes of water in cells were excited and probed in a time-resolved fashion [66], as shown in Fig. 3.4. The first demonstration of SRS as a contrast mechanism for *imaging* followed several years later, in the form of broadband SRL and SRG using a white light probe pulse and a modulated, spectrally narrow pump pulse [59]. In the configuration as used by Freudiger et al., two input beams at frequencies ω_p and ω_s and picosecond pulsewidth are tuned to match a vibrational mode of interest in the sample [60]. The first application of picosecond SRS microscopy to biological systems is reproduced in Fig. 3.5. However, in all these cases, the SRS signal cannot be spectrally isolated from the input beams. This necessitates the use of modulation techniques, wherein a modulation applied to one beam is transferred onto the SRS signal imprinted onto the other beam. One enabling factor for SRS microscopy was selecting a modulation frequency that is high enough such that the $1/f$ noise from the laser is minimized, resulting in modulation frequencies of >1 MHz [67]. Using variations on these techniques, concentrations as low as 100μM have been demonstrated [68, 69].

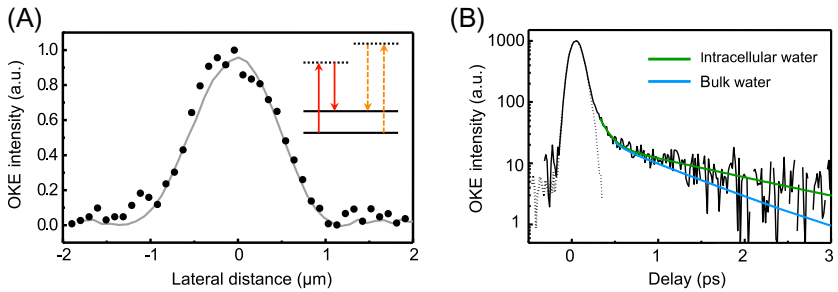

FIG. 3.4 Stimulated Raman scattering microspectroscopy with a high numerical aperture objective. (A) Optical Kerr effect signal of a 1 μm diameter glass bead as it is scanned through focus. *Inset* shows a Jablonski diagram with the femtosecond pump (*red*) and probe (*orange*) field interactions indicated. (B) Impulsive optical Kerr effect microspectroscopy of water inside a live cell (*black curve*). A fit reveals a structural relaxation time of 1.35 ps for cell water (*upper fit line*) and a relaxation time of 0.79 ps for water of the growth medium (*lower fit line*). *(Adapted with permission from E.O. Potma, W.P. de Boeij, D.A. Wiersma, Femtosecond dynamics of intracellular water probed with nonlinear optical Kerr effect microspectroscopy, Biophys. J. 80 (6) (2001) 3019–3024, https://doi.org/10.1016/s0006-3495(01)76267-4.)*

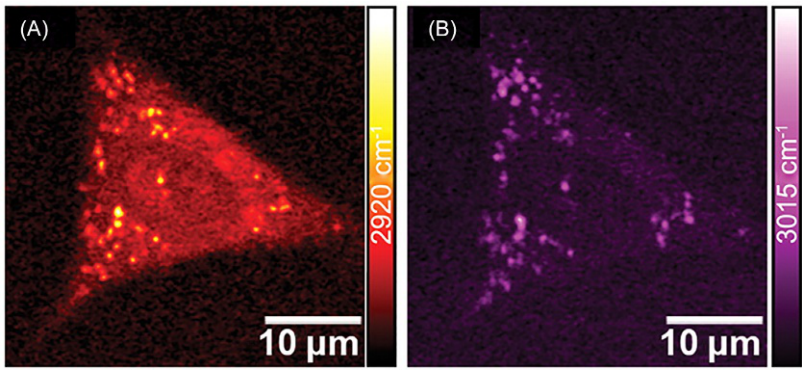

FIG. 3.5 SRS is shown to be a powerful tool to image lipid distribution for cell cultures and tissues in the first biological SRS microscopy report. Here, Omega-3 fatty acid uptake is monitored in A549 human lung cancer cells. (A) SRL image taken at 2920 cm^{-1}. (B) SRL image of the same cell taken at 3015 cm^{-1} which is indicative of unsaturated fatty acids. *(Reproduced with permission from C.W. Freudiger, W. Min, B.G. Saar, S. Lu, G.R. Holtom, C. He, J.C. Tsai, J.X. Kang, X.S. Xie, Label-free biomedical imaging with high sensitivity by stimulated Raman scattering microscopy, Science 322 (5909) (2008) 1857–1861, https://doi.org/10.1126/science.1165758. Copyright 2008 American Association for the Advancement of Science.)*

While these advances in sensitivity are already commendable, the resulting molecular concentration limit is still higher than the intracellular concentration of many small metabolites, with concentrations in the μM range being typical. In addition, Raman scattering cross sections of the vibrational modes of biomolecular molecules are inherently low (in the 10^{-28}–10^{-32} cm^2/sr range). Several groups have turned to developing other ways of boosting the SRS signal. Of particular note is the use of electronic resonance conditions similar to that of resonant ISRS [70]. It is well known that the SRS signal can be greatly enhanced by tuning the frequency of the incident radiation to be near or at an electronic transition. By exploiting the electronic resonance, imaging of molecules at sub-μM concentrations has been reported [71–73].

Some of the underlying principles in SRS microscopy and its applications will be further discussed in Section 3.3.

3.1.5 Fourth wave: Nanoscale and single-molecule spectroscopy

Inspired by the successes of nanoscale spectroscopy and single-molecule spectroscopy techniques, the last decade has seen a growing effort by the SRS community to push the sensitivity of the technique to the nanoscale. At the nanometer level, the number of molecules is necessarily smaller, and this, in turn, affects the detectability of the signal. The Raman effect alone is too weak to allow for measurements at this level, and the effect of stimulating the Raman transition, which effectively increases the detected signal by 10^5–10^6 times, remains insufficient to enable the observation of molecules at this scale. Additional mechanisms are needed to boost the signal, and some of these mechanisms are discussed in Section 3.4.

Among the developments that pushed the SRS technology to the nanoscale, and, by extension, to the single-molecule limit, is the technique of using surface plasmons to enhance the Raman response. The fields of surface and cavity-enhanced Raman spectroscopy are well established in their own right [74–76]. Following much the same evolution from Raman to SRS, surface-enhanced Raman scattering (SERS) has been translated into the surface-enhanced stimulated Raman scattering (SE-SRS) family of techniques. While much of the advances in SE-SRS occurred in the 21st century, it was first proposed and demonstrated in 1979 at the Bell Labs [77, 78]. These techniques have been used to probe a variety of scientific problems, including the promise of creating "molecular movies" of targets in plasmonic cavities at the ultrashort timescales [79]. This technique also shows promise in studying plasmonic catalysis, for detection of small drug compounds, and of plasmonic processes in nanoaggregates. The process can also be utilized in a variation of tip-enhanced Raman spectroscopy [80]. However, these advances did not come without challenges. The high peak intensities inherent in surface-enhanced picosecond and femtosecond spectroscopies have been shown to be on the order of 1 V/nm; a regime where chemical changes in the molecules of interest may be induced by the applied fields themselves.

3.1.6 Toward SRS nanoscopy

As can be imagined, the Raman imaging community, spurred on by super-resolution techniques in other imaging fields [81], is pushing the limits of what SRS can do with the ultimate goal of developing a nanoscopy technique with single-molecule detection capabilities. This is an emerging field, and as such, much of its history is yet to be written. We will provide a brief overview of major trends here, while more details can be found in Chapter 11, which is dedicated to super-resolution SRS microscopy.

Early work toward this goal appears in theory by 2014 with a method similar to that of stimulated emission depletion microscopy (STED) [82]. Under this proposed scheme, an additional third pulse would be utilized in the form of a doughnut-shaped Stokes beam to saturate the SRS signal at and around the perimeter of the pump beam [83, 84]. In

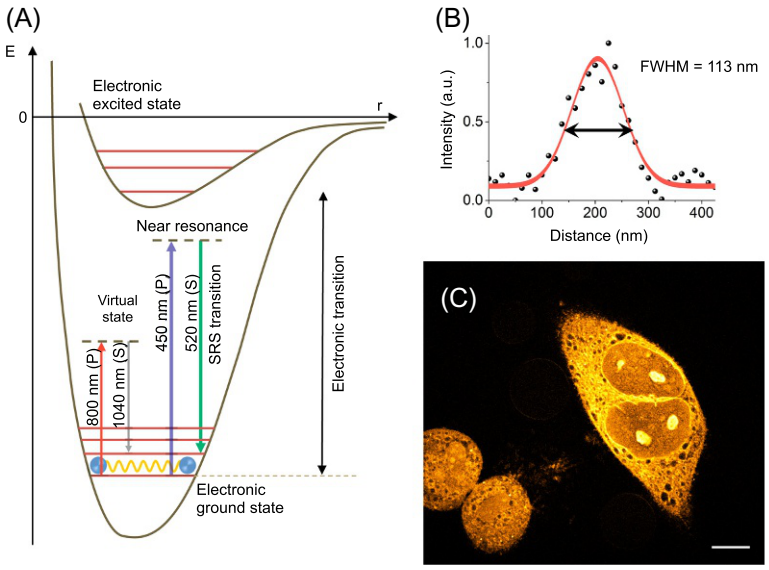

FIG. 3.6 High-resolution SRS imaging using visible pump and Stokes beams. (A) Energy-level diagram of SRS with near-infrared excitation beams, shown on the *left*, and visible excitation beams on the *right*. The near-resonant condition provides an additional boost to the signal. (B) Cross section of the SRS signal from a 60-nm polystyrene bead, showing a full width half maximum (FWHM) of 113 nm. (C) High-resolution SRS image of a cell taken with visible excitation beams. Images were obtained with a NA = 1.49 oil immersion objective lens. *(Adapted with permission from Y. Bi, C. Yang, Y. Chen, Y. Chen, S. Yan, G. Yang, Y. Wu, G. Zhang, P. Wang, Near-resonance enhanced label-free stimulated Raman scattering microscopy with spatial resolution near 130 nm, Light Sci. Appl. 7 (2018) 81, https://doi.org/10.1038/s41377-018-0082-1.)*

2015, work by Silva and colleagues demonstrated that using a STED-like approach can yield subdiffraction-level resolution [85]. In this technique, the added toroidal pulse depletes vibrational coherences in the molecules of interest by driving population away from the ground state into the vibrationally excited state, thus reducing the normal SRS signal through ground-state depletion. This effectively eliminates SRS signal generation in the overlap of the SRS coherence and the depletion beam through the process of Raman saturation. However, the low repetition rate of their laser makes this approach impractical for biological imaging. The same strategy was expanded on by Graefe et al., who demonstrated subdiffraction-limited SRS imaging with a MHz laser, which brings this technique closer to applicability in biological imaging [86]. Though it should be noted that a demonstration on a biological sample was not provided in that work. Another way to achieve the higher resolution afforded by Raman saturation is to use a special modulation/demodulation scheme that is sensitive to the nonlinear dependence of the saturation process [87]. In this fashion, no extra doughnut-shaped beam is needed, thereby significantly simplifying the experiment. This method has been used to visualize biological cells with subdiffraction-limited resolution. Among other recent efforts to improve the resolution in SRS comes a surprisingly simple solution: use shorter wavelength pump and Stokes beams and a very high-NA objective lens. Following this recipe, images of cultured cells were obtained with a lateral resolution of 113 nm [88], as highlighted in Fig. 3.6. A possible downside of this method is the increased probability of photo-bleaching and possible photo-damaging due to the use of pulsed visible light beams.

These advances demonstrate the rapid progress being made toward a true label-free vibrational nanoscopy. However, many challenges remain to demonstrate a technique fully capable of generating such visually stunning images like those currently available with fluorescence-based super-resolution techniques.

3.2 Probing molecules with SRS spectroscopy

Readers of this book with a primary interest in imaging and microscopy may be unfamiliar with the principles of SRS *spectroscopy*, the technology on which the imaging version of the SRS technique is based. In SRS spectroscopy, the emphasis is on the spectroscopic properties and physical interactions of molecules. Sample volumes in SRS spectroscopy are often in the 10 μL–1 mL range, much larger than the ~fL volumes typical for SRS microscopy. As highlighted in the earlier sections, the spectroscopy version of SRS dates back to the 1960s, the decade in which the laser was developed. With the subsequent availability of shorter laser pulses, the SRS techniques were used predominantly to offer a time-domain version of the spectra collected with spontaneous Raman scattering. The development of the ISRS technique, in particular, made it possible to follow the evolution of vibrational coherences of solids and liquids on the femto and picosecond timescales, prompting numerous research activities. In the following, we will discuss some of the properties of SRS spectroscopy, with an emphasis on the time-domain version of the technique.

3.2.1 SRS spectroscopy in the time domain

The spectra acquired in spontaneous Raman spectroscopy contain a lot of information. Besides the spectral positions and relative intensities of the Raman lines, the spectra also hold information about the dynamics of the induced Raman polarization. The longer the polarization is able to retain its induced oscillatory motion, the narrower the Raman spectral profile. Vice versa, shorter-lived Raman polarizations give rise to broader linewidths. The frequency and time domain are related to one another by a Fourier transformation. However, while the frequency-domain reports on the overall timescales on which the Raman polarization unfolds, it does not provide a time consecutive picture of the evolution of the vibrational motion. In the time domain, on the other hand, the vibrational dynamics are resolved directly as function of time, revealing the actual chronology of the vibrational movements involved. The ability to "see" the motion of chemical bond vibrations is rather compelling, and it has led to the development of a broad arsenal of time-resolved SRS techniques.

To describe the SRS experiments in the time domain, it is helpful to invoke the quantum mechanical picture of the material states while the light fields are treated classically [89]. In general, we may write the eigenstates of the molecular system as $|n\rangle$. A useful tool in describing evolution of the system as it interacts with the incident fields is found in the so-called density matrix operator. It is defined as

$$\hat{\rho}(t) \equiv \sum_{nm} \rho_{nm}(t) |n\rangle\langle m| \tag{3.1}$$

The diagonal elements of the density matrix operator, ρ_{nn}, give the probability that the molecule is in state $|n\rangle$, whereas the off-diagonal elements describe the system as it is in a coherent superposition of states $|n\rangle$ and $|m\rangle$. The operator $|n\rangle\langle m|$ is called a *coherence* when $n \neq m$, and $\rho_{nm}(t)$ gives the time-dependent amplitude of this coherence. When $n = m$, the operator $|n\rangle\langle n|$ is referred to as the system's *population* of state $|n\rangle$. In this case, the system is not in a superposition of states, but resides in a well-defined eigenstate. It is the evolution of $\hat{\rho}(t)$ that we are interested in, as it conveniently describes the light-induced couplings between the material's states and the subsequent dynamics that follows.

To follow the evolution of the system, it is convenient to consider the four-level system sketched in Fig. 3.7A. Here, the ground state is indicated as $|a\rangle$, the first vibrationally excited state as $|b\rangle$, and two virtual states as $|n\rangle$ and $|n'\rangle$. Note that the virtual states are not eigenstates of the material and thus the system cannot evolve in such states any longer than dictated by the time uncertainty in the experiment. In the semiclassical description of SRS, the material is subjected to three interactions with incoming fields. Before any field interactions, the system is in the ground-state population, expressed by the operator $|a\rangle\langle a|$. Each field interaction can change the bra or the ket of the density matrix operator.

In the time-domain SRS experiment, the first two field interactions are with a pump and probe field, indicated by E_1 and E_2, respectively, in Fig. 3.7A. These two field interactions can manipulate $\hat{\rho}$ in many ways, but here we will focus on a particular manipulation, or pathway, that forms a dominant contribution to the SRS signal. This pathway is represented in terms of a double-sided Feynman diagram in Fig. 3.7B, which is read from bottom to top. Starting in population $|a\rangle\langle a|$, both the pump (ω_1) and the Stokes ($-\omega_2$) interact on the bra side, producing the coherence $|a\rangle\langle b|$. After the preparation step, the system will evolve in this superposition of two vibrational states (Raman coherence) during time τ as the molecule interacts with its surroundings. Two important effects can alter the amplitude of the coherence. First, the vibrational lifetime of $|b\rangle$ limits the time the superposition of states can be maintained, resulting in a decaying coherence with a rate of γ_{bb}. Second, because each molecule is affected by its immediate surroundings differently, the phase evolution of the superposition of states in one molecule will differ from that of another molecule. This implies that the amplitude of the total Raman coherence in the sample will decrease as individual components run out of phase. This effect is known as pure dephasing of the coherence of the molecular ensemble, and characterized by the dephasing rate $\hat{\gamma}_{ab}$. The joint effect of vibrational lifetime and intermolecular dephasing gives rise to an overall decay rate $\gamma_{ab} = \gamma_{bb}/2 + \hat{\gamma}_{ab}$ for the Raman coherence. Here,

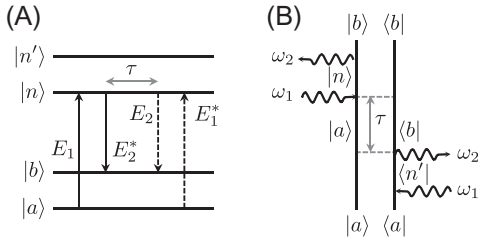

FIG. 3.7 (A) Energy level diagram with four material states, and four *field* interactions. (B) Double-sided Feynman diagram of one of the contributions to the SRS signal. Time τ indicates the time delay between the preparation and probing step in the time-resolved SRS process.

the γ_{bb} is divided by 2 because the populated decay rate is defined through the modulus square of the density matrix amplitude as $|e^{-\gamma_{bb}t/2}|^2 = e^{-\gamma_{bb}t}$.

After an evolution period τ, the system is probed by a third field interaction, here with the pump field ω_1 that interacts from the left with the ket, as shown in Fig. 3.7B. During this interaction time, the system radiates a photon at ω_2, upon which the material is left in the population $|b\rangle\langle b|$. The end result is that the system is in a higher-energy state because of the Raman interaction. The radiation probability of the ω_2 photon in the probing step is related to the amplitude of the density matrix operator after three incident field interactions. Computationally, the density matrix can be determined using third-order perturbation theory, yielding $\hat{\rho}^{(3)}(t)$, which in turn can be used to calculate the third-order polarization in the material:

$$P^{(3)}(t) = N \operatorname{tr}\left[\hat{\mu}\hat{\rho}^{(3)}(t)\right] \tag{3.2}$$

where N is the number density of molecules, $\hat{\mu}$ is the dipole operator, and the tr symbol indicates the trace over the matrix elements of the operator product between the brackets. This procedure thus gives access to the temporal evolution of $P^{(3)}(t)$, which is the key quantity measured in time-resolved SRS experiments. In general, the detected SRS signal S in the (broadband) detection channel (ω) can be written as [90]

$$S(\omega_i, t) = \frac{n(\omega_i)c}{4\pi} \operatorname{Re}\left\{E_s(t) \cdot E_i^*(t)\right\} \tag{3.3}$$

where $i = 1, 2$ for the pump and Stokes detection channels, respectively, and the signal field is written as E_s. Assuming far-field detection of a plane wave, the signal field is proportional to the nonlinear polarization, that is, $E_s \propto iP^{(3)}$, and the detected signal can be written as

$$S(\omega_i, t) \propto -\operatorname{Im}\left\{P^{(3)}(t) \cdot E_i^*(t)\right\} \tag{3.4}$$

In case the dynamics of $P^{(3)}(t)$ are followed as a function of the time delay between the preparation step and the probing step, then the amplitude of the polarization can be monitored as a function of τ. The measured quantity, $P^{(3)}(\tau)$, contains all the information about the frequencies of the driven vibrational modes as well as the dephasing parameters of all excited Raman lines. Note that the far-field SRS signal is sensitive to the *imaginary* part of the material polarization. Physically, the imaginary part of the material response is related to the exchange of energy between the material and the light fields. From this notion, it can be understood that the SRS signal is directly proportional to the energy gained by the material or, vice versa, the energy lost by the (combined) light fields.

3.2.2 Features of time-domain SRS

The characteristics of the time profile of the measured third-order polarization is dependent on the way that the experiment is conducted. In particular, different features can be observed as the bandwidth of the pump and Stokes pulses are changed. Typical features of the time-resolved SRS signal are shown in Fig. 3.8. In the column on the left-hand side, the real and imaginary parts of the Raman polarization are shown in the frequency domain. The gray-shaded area indicates the convolved width of the femtosecond pump (ω_1) and Stokes (ω_2) pulse pair. In panel (A), a high-frequency Raman mode at $\omega_v = 1000\ \text{cm}^{-1}$ is driven by the frequency difference ($\omega_1 - \omega_2$) of the pump and Stokes pulse pair. The spectral width of the effective driving frequency $\omega_1 - \omega_2$ is sufficient to cover the width of the Raman line, but insufficient to cover multiple lines. When another pump/Stokes pulse pair of similar duration is used to probe the induced polarization as a function of τ, the profile in panel (B) is observed. The frequency domain and the time domain are related by a Fourier transformation, and thus the exponential decay of the polarization directly corresponds to the linewidth of the excited mode.

In panel (C), the width of the $\omega_1 - \omega_2$ driving frequency is broad enough to coherently excite two nearby Raman lines. Now the induced polarization oscillates at two frequencies, which coherently beat against one another. These quantum beats are directly visible in the time-resolved SRS trace. The periodicity of the quantum beat is inversely related to the spectral difference between the two lines, whereas the linewidth of the individual bands is reflected in the overall decay of the time-dependent profile.

In Fig. 3.8E, the system is not driven by two spectrally separated pump and Stokes pulses, but rather by a single broad-bandwidth femtosecond pulse. This single pulse is broad enough to provide both the pump and Stokes frequencies for driving a low-frequency mode, shown here at $\omega_1 - \omega_2 \sim 100\ \text{cm}^{-1}$. In the spectral domain, the pulse covers all frequencies from zero to well beyond the mode of $100\ \text{cm}^{-1}$, which in the time domain corresponds to a pulse duration much shorter than the periodicity of the molecular vibration. The mode is now excited *impulsively*. Panel (F) depicts the time profile as the polarization is probed with the probe pulse of similar duration, revealing oscillations that now directly track the motion

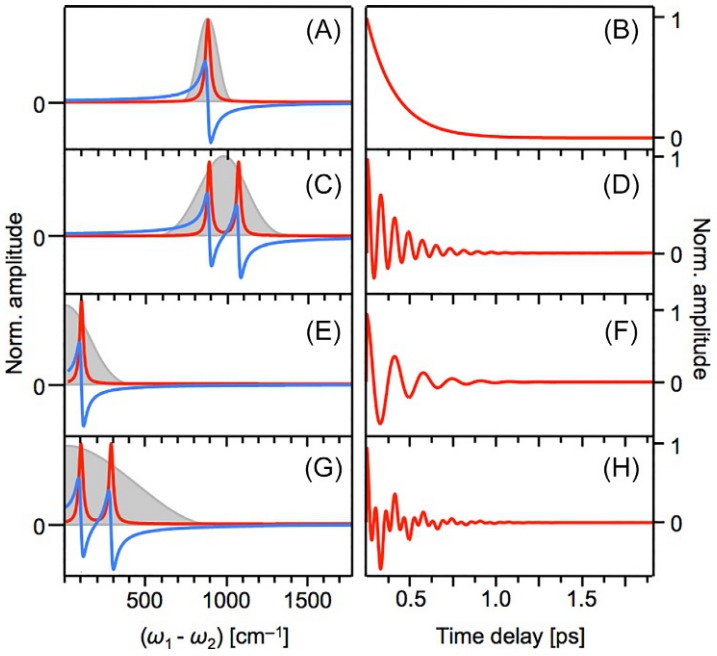

FIG. 3.8 Simulated frequency (A, C, E, F) and time (B, D, F, H) dependence of the third-order polarization $P^{(3)}$ as probed under different experimental conditions. (A) Amplitude of the real *(blue)* and imaginary *(red)* part of the nonlinear polarization due to the presence of a single high-frequency Raman resonance. The Raman coherence is driven by the pump (ω_1) and Stokes (ω_2) fields at ($\omega_1 - \omega_2$). *Gray region* indicates the spectral profile of the effective driving field ($\omega_1 - \omega_2$). (B) Amplitude of $P^{(3)}$ as a function of time delay τ, corresponding to the situation in (A). (C) Driving two high-frequency Raman resonances with two broadband laser fields in the spectral domain and in the (D) time domain. (E) Driving one low-frequency Raman resonance with one broadband laser field in the spectral domain and in the (F) time domain. (G) Driving two low-frequency Raman resonances with one broadband laser field in the spectral domain and in the (H) time domain. *(Reprinted with permission from R.C. Prince, R.R. Frontiera, E.O. Potma, Stimulated Raman scattering: from Bulk to Nano, Chem. Rev. 117 (7) (2017) 5070–5094, https://doi.org/10.1021/acs.chemrev.6b00545. Copyright 2017 American Chemical Society.)*

of the molecular vibration. Finally, in panel (G), the single preparation pulse coherently excites two low-frequency Raman modes, resulting in the time profile of panel (H). In the latter case, the time trace exhibits oscillations of the individual modes as well as quantum beats between the modes.

If the driven vibrational modes are those of the ground-state potential, then the information in the time-resolved SRS signal is directly related to that of the Raman spectrum. In this case, the time profiles can be obtained by a simple Fourier transformation of the spontaneous Raman spectrum and no new insights are to be gleaned from the time-resolved SRS measurements. This is an important realization, as there is, in principle, no reason to perform a much more complicated ground-state SRS experiment in the time domain when a simple spectral Raman measurement suffices. In many ways, earlier picosecond and femtosecond time-resolved SRS studies of ground-state vibrations, while technically important advances, have added very few new fundamental insights into the dynamics of molecules. Nonetheless, time-resolved impulsive SRS remains as an important approach for detecting low-frequency modes that are difficult to detect in the frequency domain because of their proximity to the Rayleigh line. This higher sensitivity to low-frequency modes has recently been exploited in microscopy as well, in the form of impulsive SRS microscopy, which is the topic of Chapter 7.

The information content offered through either time- or frequency-resolved Raman experiments is no longer strictly identical, however, when the molecule is excited first to an electronically excited state, and then allowed to evolve on the excited-state potential while the SRS process is used to probe vibrational motions. This scenario is relevant to a wide variety of photochemical processes. A frequency-domain measurement is unable to resolve the time consecutive steps of the wave packet dynamics, and a time-resolved measurement is the only way to fully appreciate the dynamics on the excited-state potential. An important form of SRS spectroscopy in the latter category of experiments is called femtosecond stimulated Raman scattering (FSRS), to which we will turn next.

3.2.3 Femtosecond stimulated Raman scattering (FSRS)

The FSRS approach follows a specific scheme that proved to be very favorable for studying molecular conformational dynamics after a photoinduced excitation. This situation is relevant to chromophores with electronic resonances in the visible range of the spectrum that undergo dynamic changes upon photoexcitation. Examples include photoisomerization reactions, internal conversion dynamics, and excited-state electron and proton transfer processes.

The FSRS technique involves the excitation of the target molecule by a short actinic pump pulse, which prepares a wave packet on the excited-state potential, shown in Fig. 3.9A. The actinic pulse is typically a short femtosecond pulse, which plays an important part in defining the temporal resolution of the experiment. The vibrational modes in the excited state are then probed through an SRS process as the wave packet evolves on the excited-state potential. The SRS process is achieved through a combination of a spectrally narrow Raman pump pulse and a spectrally broad probe pulse. This is a common

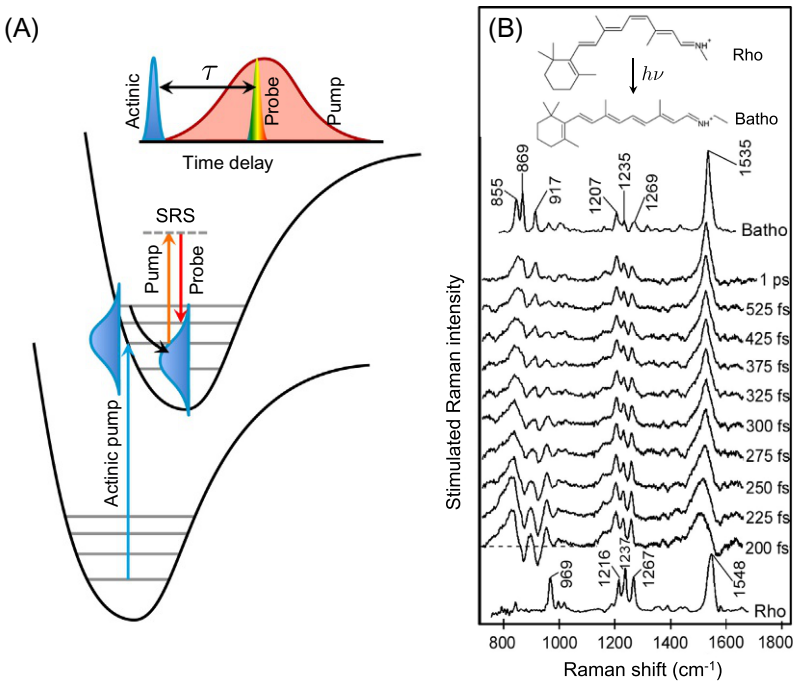

FIG. 3.9 (A) The FSRS excitation scheme where a fs actinic pulse prepares a wave packet on the excited state, which is subsequently examined by SRS spectroscopy as it evolves on the potential surface. *Inset* shows the time domain picture. (B) Application of FSRS to the photoisomerization of 11-cis retinal in rhodopsin to the all-trans bathorhodopsin photoproduct. Time-resolved FSRS spectra are shown for different delay times τ between the actinic pulse and the SRS pump pulse. Resonance Raman spectra of ground-state rhodopsin (Rho) and the trapped bathorhodopsin (Batho) product are included for comparison. *(Adapted with permission from P. Kukura, D.W. McCamant, S. Yoon, D.B. Wandschneider, R.A. Mathies, Structural observation of the primary isomerization in vision with femtosecond-stimulated Raman, Science 310 (5750) (2005) 1006–1009, https://doi.org/10.1126/science.1118379.)*

scheme for acquiring SRS spectra, as the spectral resolution $\Delta\nu$ is determined by the narrow Raman pump pulse, which imprints narrow SRL and SRG features onto the broadband probe, as well as the resolution of the spectrometer that is used to collect the spectra. In the time domain, the Raman pump pulse duration is in the picosecond range, while the probe pulse is in the sub-100 fs range. Time delaying the probe pulse relative to the actinic pulse will allow the collection of SRS spectra at different time points as determined by the time delay τ of the actinic pulse and the probe pulse, both of which are in the femtosecond range. The cross correlation between these short pulses sets the time resolution Δt along the τ-axis. The long picosecond pulse envelope of the Raman pump is virtually flat over the examined time delay and is thought not to limit the time resolution of the experiment. In this fashion, vibrational spectra with a spectral resolution of $\Delta\nu \sim 10\ \text{cm}^{-1}$ have been recorded with a temporal resolution of $\Delta t \sim 100$ fs as the photo-physical process on the excited-state potential unfolds.

The principle of FSRS was first developed in 1994 [91]. Subsequent improvements showed the utility of the approach for following the photoisomerization of a dye molecule, the conformational dynamics of β-carotene, and the isomerization of retinal chromophores [55, 92]. Ever since the early 2000s, the FSRS technique has been applied to numerous other molecular systems [56, 93]. An example of the power of FSRS is shown in Fig. 3.9B for the case of 11-cis retinal in rhodopsin, a study that uncovered the primary structural changes of the chromophore responsible for vision.

As can be seen in Fig. 3.9B, the vibrational features of the FSRS Raman gain spectra display changes on the $<$100 fs timescale, suggesting that simultaneous high Δt and $\Delta\nu$ can be achieved. This is remarkable, as the time-bandwidth product $\Delta t\Delta\nu$ in a typical optical experiment is constrained by the Fourier relationship between the conjugated variables of time and frequency. For instance, for optical experiments conducted with Gaussian pulses, the time-bandwidth product is found as $\Delta t\Delta\nu \approx 15$ ps/cm. In FSRS, time-bandwidth products of 1 ps/cm or lower have been reported [94], raising questions about violation of the fundamental uncertainty between time and frequency. The argument that the delay time τ and the spectral resolution on the spectrometer are independently controllable parameters, and thus not Fourier conjugates, seeks to dispel such concerns.

However, others have pointed out that it is not the system's evolution along the τ dimension that is of direct relevance to the time-bandwidth product of the vibrational lines, but rather the time evolution of the system during the generation of the stimulated Raman gain photons [95]. For these photons to acquire a narrow spectral width of $10\ \text{cm}^{-1}$, the light-matter interaction must have a duration of $\sim$1.5 ps for this spectral content to develop. During this interaction time with the Raman pump and probe pulses, the wave packet would sample different parts of the excited-state potential. In this scenario, dynamics can still be observed on shorter timescales, but the vibrational part of the time-dependent polarization needs a longer time to develop its signatures and, thus, cannot be resolved with the same Δt as the electronic contributions to the polarization. Despite these concerns, theoretical methods have been developed that promise to retrieve the dynamic

peak frequencies of the relevant Raman modes from the FSRS spectra on a timescale much faster than the time needed to develop a narrow line [96].

3.3 Probing smaller samples: The transition to microscopy

As alluded to in Section 3.1, the use of SRS as a contrast mechanism for microscopy has been a fruitful area of scientific research and engineering over the last two decades. Getting to that point, however, required significant work in the realm of spectroscopy, and several important realizations and considerations about the spatial nature of light propagating in smaller and smaller interaction volumes.

3.3.1 Shrinking the probing volume

As discussed in Section 3.2, the experimental configuration for SRS changes quite dramatically when moving from a typical SRS spectroscopy experiment to an SRS measurement in an optical microscope. One of the most striking and important differences that occur between these configurations is the size and form of the probing volume. In a typical ISRS experiment, the pump and probe beams are incident on the sample at different angles, forming an overlap region that constitutes the interaction volume. Typically, the interaction length is on the order of 0.1–10 mm. The interaction volume is orders of magnitude larger than the optical wavelength, and the nonlinear polarization radiates a signal in a well-defined, phase-matched direction. The issue of phase matching is important in both SRS spectroscopy of bulk samples as well as in SRS microscopy, albeit in different ways.

Spatial phase matching is an important consideration for all coherent nonlinear optical experiments. In SRS, phase matching describes the process of matching the spatial phase of the induced polarization $P^{(3)}$ to that of the propagating signal beam. Each field ω_i involved in the SRS interaction is described with a spatial phase $\phi_j = \mathbf{k_j}\cdot\mathbf{L}$, where k_j is the associated wavevector and $\mathbf{L}$ is the vector describing the propagation distance inside the interaction volume. The three incident fields that drive $P^{(3)}$ assign a spatial phase to the induced polarization. In SRL, the nonlinear polarization is driven by the effective driving field $E_1(\mathbf{r})E_2^*(\mathbf{r})E_2(\mathbf{r})$, whereas in SRG the effective driving field is $E_2(\mathbf{r})E_1^*(\mathbf{r})E_1(\mathbf{r})$, resulting in the following spatial phases:

$$\phi_{SRL} = (\mathbf{k}_1 - \mathbf{k}_2 + \mathbf{k}_2)\cdot\mathbf{L} \tag{3.5}$$

$$\phi_{SRG} = (\mathbf{k}_2 - \mathbf{k}_1 + \mathbf{k}_1)\cdot\mathbf{L} \tag{3.6}$$

The spatial phase of the nonlinear polarization needs to match that of a propagating beam at the signal frequency, which in the case of SRS corresponds to the phase of the (forward propagating) probe beams. For SRL, the phase required to generate a propagating beam at ω_1 is $\phi_{\omega_1} = \mathbf{k_1}\cdot\mathbf{L}$, and for SRG the required phase is $\phi_{\omega_2} = \mathbf{k_2}\cdot\mathbf{L}$. The phase difference $\Delta\Phi$ between the induced polarization and the probe field is then given as

$$\Delta\Phi_{SRL} = \phi_{SRL} - \phi_{\omega_1} = (\mathbf{k}_1 - \mathbf{k}_2 + \mathbf{k}_2 - \mathbf{k}_1)\cdot\mathbf{L} = \Delta\mathbf{k}\cdot\mathbf{L} \tag{3.7}$$

$$\Delta\Phi_{SRG} = \phi_{SRG} - \phi_{\omega_2} = (\mathbf{k}_2 - \mathbf{k}_1 + \mathbf{k}_1 - \mathbf{k}_2)\cdot\mathbf{L} = \Delta\mathbf{k}\cdot\mathbf{L} \tag{3.8}$$

In Eqs. (3.7), (3.8), $\Delta\mathbf{k}$ is defined as the wavevector mismatch. In general, if $\Delta\Phi > \pi$, the radiation originating from the induced polarization cannot propagate into the far field. It is serendipitous that for both SRG and SRL experiments $\Delta\mathbf{k} = 0$ and consequently $\Delta\Phi = 0$. In other words, there is no phase mismatch between the induced polarization and a propagating signal field. The signal is said to be phase matched in the forward propagation direction of $\mathbf{k_i}$. For homogeneous bulk samples, $\mathbf{L}$ is very long compared to an optical wavelength, so $\Delta\mathbf{k} \approx 0$ is a crucial condition. Importantly, in the backward direction, the wavevector of the propagating signal field is $-\mathbf{k}_i$, and it can be seen that $\Delta\mathbf{k}\neq 0$ for both SRG and SRL. Consequently, even for small $\mathbf{L}$ the total phase difference $\Delta\Phi$ easily surpasses π, resulting in a complete phase mismatch and thus no signal in the backward direction.

3.3.2 Phase matching in coherent Raman microscopy

While the previous section focuses on the wavevector mismatch, $\Delta\mathbf{k}$, the full equation for the phase difference, $\Delta\Phi = \Delta\mathbf{k}\cdot\mathbf{L} < \pi$, leaves open the possibility of experimental conditions where the earlier criterion can be satisfied even if the wavevector mismatch is nonzero. This becomes highly relevant in the case of microscopic probing volumes. In a typical SRS microscopy setup, the pump and Stokes beams propagate collinearly and are not spatially separated. As stated earlier,

in the forward direction $\Delta\mathbf{k} = 0$, yet in the backward direction $\Delta\mathbf{k} \gg 0$ and we might expect an absence of detectable signal on an epi-direction detector. However, the beams are focused by an objective lens to a very small focal volume. For a high numerical aperture objective, $\mathbf{L} \sim 1$ μm, on the order of an optical wavelength. If the focal volume contains very small objects, then the interaction distance $\mathbf{L}$ can be very small such that the condition $\Delta\mathbf{k} \cdot \mathbf{L} < \pi$ is met for backward-radiated fields [97, 98]. Hence, unlike in SRS spectroscopy of bulk samples, in SRS microscopy situations exist where phase-matched signal can be detected in the epi-direction as well.

Another difference between regular SRS spectroscopy and SRS microscopy is how the signal is modeled. In SRS spectroscopy, the propagating fields are assumed to be plane waves and the signal is commonly described by the one-dimensional (1D) nonlinear wave equation. This approximation is no longer valid when describing the signal in SRS microscopy. The wave front passing through the objective lens spans a wide distribution of propagation angles, which are needed to form a tightly focused interaction volume. This negates the use of the 1D wave equation as a tool for modeling signal generation. In addition, a collimated beam with a linear transverse polarization will be transformed by the focusing lens to produce a focal field with nonnegligible polarization components along both the transverse and longitudinal dimensions [99]. To further complicate the matter, the Gouy phase shift becomes manifest over a distance similar to an optical wavelength under microscopic focusing. These distinctions from macroscopic SRS have led to the development of a different class of models to describe the generation and propagation of the SRS signal from microscopic volumes. A more intuitive approach is to model the sample as an ensemble of dipole emitters driven nonlinearly by the excitation fields. The radiation generated by the dipoles can be collected in the far field, and the magnitude and direction of the signal computed as a function of particle size, shape, position, and other material properties [90, 98].

3.3.3 Instrumentation for SRS microscopy

Despite the difficulty in modeling, SRS experiments at the microscopic level have proven to be feasible and practical. The field of SRS microscopy is flourishing especially in its use to image and study biological samples. The traditional appeal of the technique is its ability to generate label-free, chemically specific samples. Experiments are often conducted with near-infrared beams, such that sample heating and photodamage is generally not a concern. As a multifaceted tool, it is capable of imaging tissues, cell cultures in both monolayer and three-dimensional (3D) form, and molecular distribution inside single cells. In this section, we examine the common instrumentation builds utilized in SRS microscopy (Fig. 3.10).

SRS systems and experiments can be divided into two broad categories based on the laser being used: (1) broadband techniques, using a femtosecond laser, or (2) narrowband techniques, which typically make use of a picosecond laser. In an SRS experiment, the two light fields, pump ω_1 and Stokes ω_2, must be supplied in a synchronized manner. This can take the form of two synchronized lasers, a laser and an optical parametric oscillator (OPO), or a single laser whose output is split and modified in some way.

The major difference between broadband SRS and narrowband SRS is in how the condition $\omega_v = \omega_1 - \omega_2$ is fulfilled. In SRS microscopy, the Raman-active mode, ω_v, is the source of contrast. In narrowband, or frequency-tuned, SRS

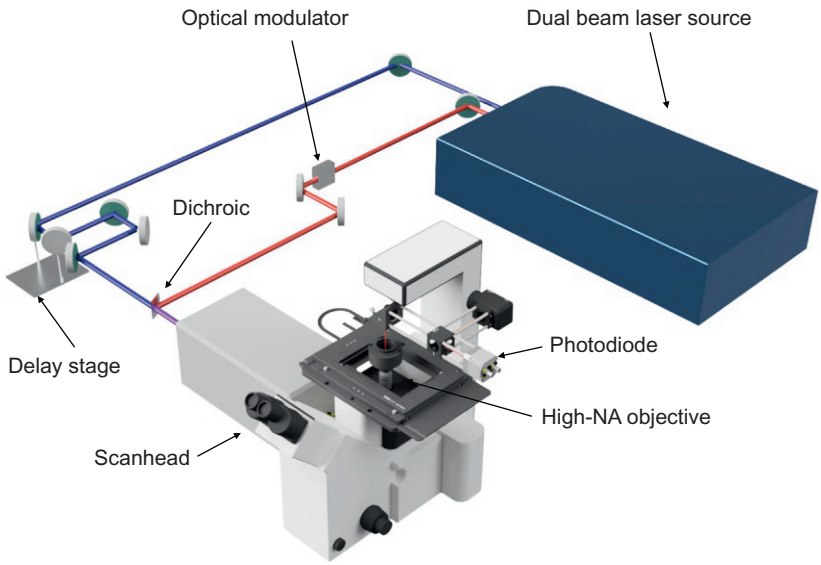

FIG. 3.10 A typical SRS setup with two synchronized beams. During the SRS process, the modulation applied to one beam is transferred to the other. The signal can then be demodulated with a lock-in detector.

experiments, a picosecond light source with a repetition rate near 80 MHz is commonly used. The light source is coupled with an OPO, which allows one of the two beams to be tuned such that ω_v can be selected. The other beam may be provided by a second laser output, through residual OPO-pump light, or from the idler beam of the OPO depending on the specifics of the setup. After one of the beams is modulated—pump for SRG, Stokes for SRL—the beams are spatially and temporally overlapped. The overlapped beams are raster scanned through a high-NA objective incident onto the sample. From there, the output beams are spectrally filtered to remove the originally modulated beam, and the one carrying the SRS signal is detected. In this setup, the choice of the variable wavelength beam is the determining factor in what Raman mode is probed. The narrow spectral bandwidth of picosecond pulses gives rise to the ability to be highly selective of which mode is probed. For hyperspectral imaging, multiple images—each at a different wavelength—are acquired and analyzed. The downside of this method is that spectrally tuning is generally a slow procedure, so obtaining a relatively wide spectrum of images is time consuming. In addition, the relatively low peak power of picosecond pulses compared to femtosecond pulses reduces the overall signal.

For broadband SRS microscopy, the technique can be further separated into two distinct methodologies: shaping techniques and the multiplex techniques [100, 101]. Two different but similar approaches are used to shape pulses for SRS microscopy, namely pulse shaping and spectral focusing. In both techniques, the output of a femtosecond laser is shaped to improve the spectral resolution of the experiment. In the pulse shaping technique, a 4-f pulse shaper, consisting of a grating and a motorized slit or spatial light modulator, is employed to spectrally shape either the Stokes or pump beams, or both. In one implementation, a pulse shaper picks a color out of a broadband femtosecond pulse. By holding one line at a constant wavelength, the other can be quickly scanned to allow for rapid spectral imaging. Nonetheless, this method presents some difficulties, as it adds complexity to the setup and requires high-output power from the laser source as only a small percentage of the total light in each pulse makes it to the sample. More information on pulse shaping in SRS microscopy can be found in Chapter 9. In the spectral focusing technique, adequate spectral resolution is created by positively chirping both the pump and Stokes beam. This creates a quasilinear distribution of frequencies as a function of time. By scanning the time delay of one beam relative to the other, the difference frequency for driving a specific Raman mode is selected. This method is easier to implement than pulse shaping; however, the spectral resolution is relatively low, $\sim$20 cm^{-1} in practical applications.

In multiplex SRS microscopy, a combination of broadband and narrowband pulses is used. The combination of the two pulses excites multiple Raman modes simultaneously. This idea is similar to what is used in SRS spectroscopy. However, whereas in spectroscopy applications, a spectrometer is used for resolving the spectral components, such an approach is too slow for signal collection in microscopy. For this purpose, alternative detection strategies have been developed. In one such scheme, the pump beam is spectrally dispersed and the various wavelengths are amplitude modulated at distinct frequencies. The beam is recombined and overlapped with a narrowband Stokes beam. After interaction with the sample, the SRS signal is encoded onto the Stokes with distinct frequency components. The signal is recorded by a single photodiode in the time domain. A Fourier transform of each pixel will then give rise to the SRS spectrum [102–104]. Many other strategies exist for capturing the SRS spectrum. One implementation involves spectrally dispersing the detected beam onto a photodiode array with either tuned or resonant amplifiers or multichannel lock-in detectors for demodulation of each spectral component [105–109].

3.3.4 Applications of SRS microscopy

The broad array of instrumentation types as well as abilities conferred by the nature of nonlinear microscopy allow SRS to be deployed to a wide array of use cases. While we attempt to highlight these cases here, the reader is also referred to Chapters 27–35 of this book as well as a number of review articles on the subject of SRS microscopy [100, 110–113]. With an axial resolution of approximately 1 μm, SRS offers excellent optical slicing capabilities for 3D imaging. For certain cases, the signal generation efficiency is high enough to enable video-rate imaging in biological samples [114]. This corresponds to a frame rate of 30 frames per second and a pixel dwell time around 100 ns. Like other microscopy techniques, multiple SRS images can be combined and overlapped to produce mosaics of tissue samples several centimeters in diameter [115, 116]. Some examples of the myriad uses of SRS microscopy are shown in Fig. 3.11.

Perhaps the area where SRS microscopy has really stood out is in metabolic imaging through the use of hyperspectral and multiplex acquisition and analysis. By producing images targeting different Raman modes, chemically informative maps can be produced and quantitative measurements made. Lipid mapping and lipid-to-protein ratios are a mainstay of SRS microscopy [117–125]. The 3015 cm^{-1} band associated with C=C–H stretching modes in unsaturated fatty acids and the CH_2 stretching mode of lipids at 2845 cm^{-1} provide excellent sources of contrast. Of particular note, these bands were used to follow in vivo myelination of tadpoles [126]. They have been used to image various fatty acids in multiple

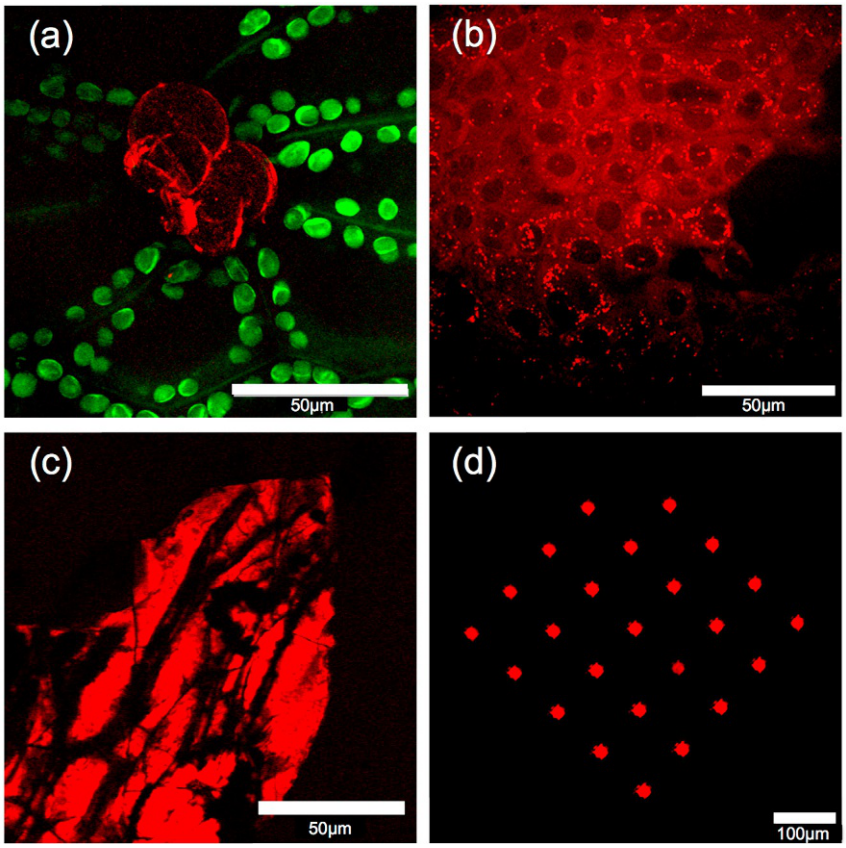

FIG. 3.11 Examples of SRS imaging of various samples in the high-frequency range (2000−3300 cm^{-1}). (A) Lipid-secreting gland of *Drosera capensis* at 2845 cm^{-1} *(red)* and pump-probe signal from the surrounding chloroplasts *(green)*. Sample courtesy of Jessica Kelz (UC Irvine). (B) Lipid droplet distribution in cultured rabbit meibocytes at 2845 cm^{-1}. Sample courtesy of Dr. James Jester (UC Irvine). (C) Crystallized d38-cholesterol crystal imaged at 2140 cm^{-1}. (D) Polymer cubes printed with two-photon polymerization visualized at 2900 cm^{-1}.

types of cancer cells. Protein and nucleic acid distributions can also be distinguished inside cells and within the extracellular matrix [127, 128].

One of the earliest demonstrations of SRS was performed on human lung cancer cells. This work provided a prelude to the extensive use of the technique for studies of various kinds of cancers including breast cancer [129, 130], skin cancers [131], brain tumors [132, 133], and gastrointestinal tumors [134]. The reader is directed to Austin et al. for a more thorough review of SRS applications in cancer diagnostics [135]. SRS has also proven useful in other areas of biomedicine. It can be used to characterize vascular structure and atherosclerotic plaques [136–138], as well as monitor a host of other pathologies [139–147].

In addition to using the intrinsic contrast of native biomolecules, much work has recently gone into using small-molecule Raman tags such as carbon-deuterium bonds (C–D), alkyne tags (C≡C), the carbon-fluoride bond (–C–F), azides ($-N_3$), nitriles (–C≡N), and isonitriles (–N≡C) [140, 148–157]. These various tags have Raman modes with frequencies that occur in what is commonly called the cell-silent region of the Raman spectrum between ∼2000−2700 cm^{-1}. The use of deuterium labeling has been developed to allow tracing of lipogenesis from glucose, protein metabolism, and other small precursor molecules [158–162]. It has been shown to have little to no adverse biological effects even to a high percentage of use [151, 163, 164]. In addition to the use of small functional group tags, other reporter molecules with unique Raman signatures have been developed for both the Raman microspectroscopy community and SRS imaging [165–169]. The development of bioorthogonal tags and their use in SRS microscopy is an emerging and promising field in its own right. It is expounded in Chapters 19–22 of this book.

While all the earlier applications focus on biology or disease, SRS has also found a niche in research on materials, biofuels, plant research, and pharmaceutical analysis. In the realm of materials science, SRS has been used alongside other methodologies to study microstructures in two-photon polymerization additive manufacturing [170, 171], as well as crystal orientation and more basic research [172–174]. Research into plant materials has been demonstrated several times with algae, lignin, and cellulose for biofuels and other purposes [103, 175–179]. In addition, SRS microscopy has been used to study the delivery, release and breakdown of drugs [180–186].

While the field of SRS microscopy is barely a decade old, it has resulted in a large number of publications and meaningful impacts across a variety of fields. Researchers are actively developing new techniques, new tags, and examining new systems. As these technologies mature, SRS is sure to serve as an impactful and fruitful tool for new discoveries in the microscopist's workbench.

3.4 From ensembles to single molecules

The success of SRS microscopy, where sample volumes are orders of magnitude smaller than in regular SRS spectroscopy, suggests that further reduction of the sample volume might be possible. This notion has raised the prospect of pushing SRS microspectroscopy all the way to the single-molecule limit. In this section, we will discuss work that explores the possibility of single molecules SRS and its tentative applications.

The transition from small microscopic volumes to single molecules is quite a leap. For instance, a tightly focused laser beam with a high numerical aperture objective reaches effective excitation volumes of ~0.1 fL. When this light is focused in aqueous media, the focus roughly encompasses 3.3×10^9 water molecules. The signal from a single water molecule can thus be expected to be several billion times less than the SRS signal measured in a microscope when the sample is bulk water—signals that are many order of magnitude below practical detection levels. Clearly, to reach single-molecule detection levels, regular SRS microscopy techniques come up short. Some form of enhancement is needed to lift the SRS signal from single molecules to detectable levels. Currently, two mechanisms for signal enhancement are actively explored: (1) the enhancement of the Raman cross section through electronic resonances in the molecule and (2) enhancement through confining the electromagnetic modes to nanoscopic volumes, reaching the molecular size.

3.4.1 Enhancing SRS with electronic resonances

As discussed in Section 3.2, the use of an electronic resonance in the molecule to enhance the response is a well-known strategy to improve the sensitivity and selectivity of the SRS signal. Similar to the resonance Raman effect, stronger SRS signals can be expected when the frequency of the pump beam is tuned close to an electronic resonance. This mechanism is sketched in Fig. 3.12A. In addition, the vibrational mode needs to be coupled to the electronic transition in order to maximally benefit from the electronic enhancement. Usually, this condition is met for vibrational modes closely associated with the π-conjugated network of the molecule, such as the C=C vibrations of bonds that are directly implicated in the electronic transition. The effective Raman cross section of such vibrational modes can be up to six orders of magnitude higher than for similar modes that lack the benefit of electronic enhancement. Resonance-enhanced SRS has been extensively used to study the vibrational dynamics of chromophores in solution, and has recently also been used in SRS microscopy. By choosing or designing optimal chromophores and tuning the excitation wavelength of the incident beams on or near the electronic resonance, effective enhancements of the SRS signal by 10^6 have been reached [71, 72, 187]. In combination with microscopic focusing, resonance-enhanced SRS signals of as little as ~500 molecules have been detected [73].

Whereas the well-known strategy of resonance-enhanced SRS has reached impressive sensitivities, comfortably reaching the single-molecule limit with this approach remains a challenge, and it remains to be seen how practical the method is for SRS measurements of individual molecules. This notion has prompted the development of alternative methods that leverage the strong response of electronic transition in molecules. Inspired by fluorescence-encoded infrared absorption spectroscopy, the recent efforts have focused on using the mechanism of SRS-assisted fluorescence as an effective means to perform vibrational measurements on molecules that exhibit strong fluorescent emission. In this approach, a vibrational state is first populated in the ground-state potential through the SRS mechanism and subsequently

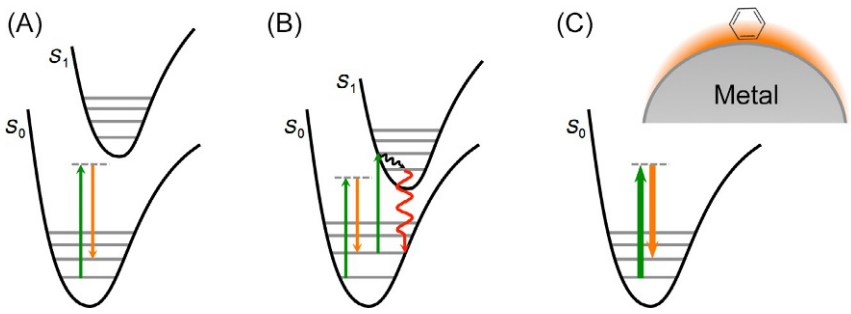

FIG. 3.12 Different forms of electronic enhancement of the SRS signal. (A) (Pre)resonant SRS. The molecular Raman polarizability is enhanced by an electronic resonance of the molecule. (B) Stimulated Raman excited fluorescence (SREF). An SRS process in the ground state is followed by an excitation to the excited state of a fluorophore, followed by fluorescence emission. (C) Surface-enhanced SRS. The transition rate in the molecule is accelerated by the presence of enhanced local excitation fields, provided by a plasmonic antenna.

probed by exciting the molecule to an electronically excited state with an additional light-matter interaction. The fluorescence that follows is then a measure of the successful population of the vibrational state [188]. This process is illustrated in Fig. 3.12B. The beauty of this approach is that it takes maximally advantage of the efficiency of the fluorescence process. Using molecules that exhibit high fluorescence quantum yields, the fluorescence probing step can reach efficiencies close to 1, thus completely eliminating the tentative challenges of detecting the loss of a single pump photon in a regular stimulated Raman loss experiment on a single molecule. Hence, whereas stimulated Raman excited fluorescence (SREF) involves an additional molecular excitation in addition to the ground-state SRS transition, the fluorescence detection strategy is orders of magnitude more sensitive than the common SRS detection scheme. This optimization of detection scheme has led to new SRS sensitivities that were hitherto deemed impossible, enabling reproducible measurements of single molecules with good signal to noise ratios [188, 189]. This method is thus suitable for mapping fluorescent probes with a spectral resolution defined by the vibrational linewidth of the chosen marker band. On the other hand, the requirement of specific fluorophores with favorable properties for SREF renders the method unsuitable as a general approach to increase the SRS detection sensitivity for any given molecule. In this regard, methods that do not rely on the presence of electronic resonances in the target molecule remain of great interest. The most successful approach in this category is the use of nanoscale antenna systems that support plasmonic resonances, which we will discuss next.

3.4.2 Enhancing SRS with plasmonic resonances

In 1974, Fleischmann et al. made a very curious observation. They found that the spontaneous Raman signal of pyridine was much stronger if the target molecule was adhered to a roughened silver electrode [190]. Several years later, members of the Van Duyne group figured out why: the surface plasmon resonances supported by the nanostructured silver provided local fields that are strong enough to enhance the Raman response from the molecules in close vicinity to the surface [191]. Subsequent work underlined the favorable properties of localized surface plasmon resonances for surface spectroscopy [192], and Raman spectroscopy in particular [74]. Structures that support such resonances, typically made of nanostructured noble metals that display resonances in the visible range of the spectrum, act like efficient antennas in that they couple propagating radiation to strongly localized evanescent fields [193]. The spatial confinement of such surface-bound electromagnetic fields can be so effective that "hotspots" of less than a nanometer can be reached. At these scales, far below the diffraction limit of propagating light, the fields are confined to dimensions that approach the molecular size, allowing efficient coupling of the field to the charges in the molecule. Vice versa, the radiative properties of the induced polarization are enhanced by the presence of the plasmonic antenna, allowing the near-field molecular polarization to couple efficiently to the far field in the form of radiation.

In this picture of electromagnetic enhancement of the signal, the surface-enhanced Raman scattering (SERS) response can be understood as

$$S(\omega_s) \propto N\beta^2(\omega_p) I_p \beta^2(\omega_s)\sigma_s \tag{3.9}$$

where ω_s is the Stokes frequency, ω_p is the pump frequency, I_p is the pump intensity, N is the number of molecules in the illuminated volume, and σ_s is the Raman cross section. The field enhancement factor is denoted as β. Both the excitation (at ω_p) and radiation (at ω_s) processes are enhanced by a β^2 factor by the antenna, giving rise to an effective enhancement of the Raman signal by β^4. Well-designed nanoantenna systems offer β factors of well over 100 times, producing overall enhancement factors in the range $\beta^4 \sim 10^8 - 10^{12}$. Such enhancements have been shown to be sufficient to generate spontaneous Raman signals from single molecules [194–196]. Given the infamous weakness of the Raman effect, the ability to perform Raman experiments at the single-molecule level is truly a remarkable achievement, and it underscores the tremendous efficiency of plasmonic antennas to improve the optical interaction between propagating radiation and the molecule.

The success of SERS suggests that even stronger signals can be expected when surface enhancement is combined with SRS, shown schematically in Fig. 3.12C. The Raman signal of the simple picture presented in Eq. (3.9) would then be further amplified by a factor proportional to I_s, the intensity of the stimulating Stokes beam. Whereas the surface enhancement factor of the surface-enhanced SRS signal would still be β^4, the effect of the stimulating beam can be expected to increase the transition rate in the molecule by another factor of $10^5 - 10^6$. The motivation for developing surface-enhanced version of SRS is thus to collect Raman signals from low-concentration samples, down to single molecules, at much higher signal acquisition rates than what can be achieved with SERS.

As stated earlier, the first indications that the SRS process can be enhanced by surface plasmons were provided in 1979, only a few years after the SERS mechanism was established [77, 78]. In the same year, it was unambiguously shown that the

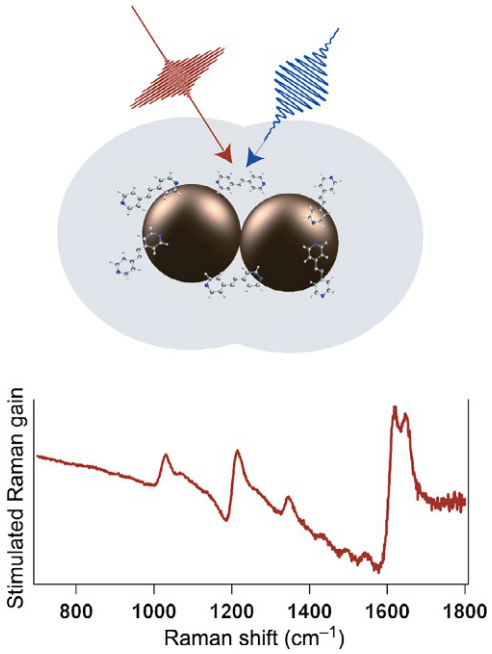

FIG. 3.13 Surface-enhanced SRS was first demonstrated on nanoantennas containing trans-1,2-bis(4-pyridyl)-ethylene molecular reporters. *(Adapted with permission from R.R. Frontiera, A.-I. Henry, N.L. Gruenke, R.P. Van Duyne, Surface-enhanced femtosecond stimulated Raman spectroscopy, J. Phys. Chem. Lett. 2 (10) (2011) 1199–1203, https://doi.org/10.1021/jz200498z. Copyright 2011 American Chemical Society.)*

surface plasmon polaritons (SPPs) provided by flat silver films were responsible for the enhancement of coherent anti-Stokes Raman scattering (CARS) from benzene molecules in close proximity to the film [197]. Despite these encouraging early indications, surface-enhanced SRS was not further pursued until much later. In 2011, interest in surface-enhanced SRS was rekindled by a femtosecond SRS study on molecules adhered to gold dimer antennas [198]. The resulting spectrum is shown in Fig. 3.13. Besides the encouraging observation that clear vibrational signatures of the molecules were visible on the spectrally resolved signal, this study also revealed a somewhat unexpected feature, namely the dispersive nature of the vibrational lines and the presence of a relatively strong pump-probe background. Subsequent studies confirmed that this observation was no fluke but rather an intrinsic property of surface-enhanced SRS.

The virtually background-free signals and the Lorentzian lineshapes that make SRS spectroscopy in many cases preferable over CARS microscopy seem no longer applicable when the SRS process is mediated by surface plasmons. Several theoretical works have attempted to explain the observed dispersive lineshapes. What is clear from the analysis is that the Raman polarization is no longer driven by the propagating field, but by the local surface plasmon field instead. The phase of the local field can differ markedly from the phase of the incident field. The local field enhancement factors are thus complex quantities that can alter the phase relation between the driving fields and the radiated polarization in the far field. This principle largely explains the trends observed in the surface-enhanced SRS signals collected in a microscope [199].

Is the surface enhancement effect sufficient to bring SRS sensitivity into the realm of single molecules? This indeed appears to be the case. Experiments in the Cheng group have focused on individual hotspots in nanosphere aggregates and have found convincing evidence that vibrational signatures from single adenine molecules can be detected [200]. Using a bianalyte method and a special denoising algorithm to improve the SRS images, reproducible spectra that can be assigned to individual molecules were obtained. Similar to previous measurements, the spectra display dispersive lineshapes on a rather strong background. It was identified that the photothermal effect was a major contributor to the background, offering hopes that improvements in experimental design can increase the SRS sensitivity for single molecules even more. More information about surface enhancement of the SRS signal is found in Chapter 23.

3.4.3 Advanced techniques: Nonoptical detection

In SRS, the coherent Raman polarization in the sample is probed through the radiation that reaches the far-field detector. Whereas in surface-enhanced SRS, the near-field interactions are amplified by the action of surface plasmon fields, the detection principle remains the same: the near-field Raman polarization is detected by the successful radiation of photons

into the far field. However, optical detection is not the only mechanism by which the Raman polarization can be examined. Several forms of nonoptical detection of SRS have emerged and they turn out to be specifically relevant for measurements at the nanoscale.

One form of probing the induced Raman polarization is by detecting the force between the oscillating charges in the molecule and the dipole in an atomically sharp tip that is placed in the immediate vicinity of the molecule. This electromagnetic dipole-dipole force is weak, typically less than a pN [201], but it is sufficient to be picked up by a modern scanning probe microscope. This principle was used to detect the stimulated Raman signal from chromophore molecules on a glass surface [202]. Using CW pump and Stokes beams, this force detection method, named photoinduced force microscopy, was able to resolve small clusters of molecules with a spatial resolution well under 10 nm.

Another form of scan probe microscopy uses the electron tunneling current between the sample and the sharp tip as the contrast parameter. In a very elegant piece of work, the Ho group recorded the changing tunneling current of a molecule bound to the surface as it flip flops under the influence of a femtosecond pulse pair [203]. The flopping rate, recorded through the current, is a function of the successful transfer of energy from the light to the molecule, that is, energy that is needed to complete the flip flop. This energy transfer is only successful if a Raman mode is excited. By time delaying the pulse pair, the Raman coherence induced by the first pulse is converted to a vibrational population only periodically by the second pulse. This results in periodic modulation of the flopping rate as a function of the time delay between the pulses. In essence, this is a time-resolved ISRS experiment detected through the tunneling current, performed on a single molecule!

The earlier examples illustrate that other sensitive techniques can be employed to study molecules on the nanoscale through the principle of the stimulated Raman effect. It is likely that nonoptical techniques, which do not suffer from the challenge of detecting a small signal relative to the intensity of the probe beam, will gain importance as efforts increasingly focus on the coherent Raman response of single molecules.

References

[1] Clarivate Analytics, Citation report for topic stimulated Raman scattering 1962–2020, Web of Science Core Collection, Clarivate Analytics, 2021. Tech. Rep.

[2] T.H. Maiman, Stimulated optical radiation in ruby, Nature 187 (4736) (1960) 493–494, https://doi.org/10.1038/187493a0.

[3] C.H. Townes, The first laser, in: L. Garwin, T. Lincoln (Eds.), A Century of Nature: Twenty-One Discoveries That Changed Science and the World, first ed., University of Chicago Press, 2003, pp. 107–112. Chapter 8.

[4] M. Göppert-Mayer, über Elementarakte mit Zwei Quantensprüngen (Ph.D. thesis), Georg-August-Universität Göttingen, 1930.

[5] P.A. Franken, A.E. Hill, C.W. Peters, G. Weinreich, Generation of optical harmonics, Phys. Rev. Lett. 7 (4) (1961) 118–119, https://doi.org/10.1103/physrevlett.7.118.

[6] W. Kaiser, C.G.B. Garrett, Two-photon excitation in CaF_2:Eu^{2+}, Phys. Rev. Lett. 7 (1961) 229–231, https://doi.org/10.1103/physrevlett.7.229.

[7] R.W. Terhune, P.D. Maker, C.M. Savage, Optical harmonic generation in calcite, Phys. Rev. Lett. 8 (10) (1962) 404–406, https://doi.org/10.1103/physrevlett.8.404.

[8] L.L.D. John Kerr, XL. A new relation between electricity and light: dielectrified media birefringent, Lond. Edinb. Dublin Philos. Mag. J. Sci. 50 (332) (1875) 337–348, https://doi.org/10.1080/14786447508641302.

[9] L.L.D. John Kerr, LIV. A new relation between electricity and light: dielectrified media birefringent (Second paper), Lond. Edinb. Dublin Philos. Mag. J. Sci. 50 (333) (1875) 446–458, https://doi.org/10.1080/14786447508641319.

[10] E.F. Kingsbury, The Kerr electrostatic effect, Rev. Sci. Instrum. 1 (1) (1930) 22–32, https://doi.org/10.1063/1.1748632.

[11] F.G. Dunnington, The electrooptical shutter—its theory and technique, Phys. Rev. 38 (8) (1931) 1506–1534, https://doi.org/10.1103/physrev.38.1506.

[12] F.J. McClung, R.W. Hellwarth, Giant optical pulsations from ruby, J. Appl. Phys. 33 (3) (1962) 828–829, https://doi.org/10.1063/1.1777174.

[13] J.P. O'Donovan, Generation of Extremely High Peak Power Optical Pulsations From Ruby Utilizing the Pulsed-Reflector Mode (Master's thesis), U.S. Naval Postgraduate School, 1962, http://hdl.handle.net/10945/12256.

[14] A. Dadieu, K.W.F. Kohlrausch, A. Hollaender, The Raman effect in organic substances and its use in chemical problems, J. Opt. Soc. Am. 21 (5) (1931) 286, https://doi.org/10.1364/josa.21.000286.

[15] J. Green, W. Kynaston, A. Lindsey, The vibrational spectra of benzene derivatives—I. Nitrobenzene, the benzoate ion, alkali metal benzoates and salicylates, Spectrochim. Acta 17 (5) (1961) 486–502, https://doi.org/10.1016/0371-1951(61)80103-3.

[16] E.J. Woodbury, W.K. Ng, Ruby laser operation in near IR, Proc. Inst. Radio Eng. 50 (1962) 2367.

[17] G.F. Smith, Research on coherent generation of optical radiation, Hughes Research Laboratories, Contract AF 33(616)-8233, 1962. https://apps.dtic.mil/dtic/tr/fulltext/u2/296785.pdf. October Tech. Rep.

[18] G. Eckhardt, R.W. Hellwarth, F.J. McClung, S.E. Schwarz, D. Weiner, E.J. Woodbury, Stimulated Raman scattering from organic liquids, Phys. Rev. Lett. 9 (1962) 455–457, https://doi.org/10.1103/physrevlett.9.455.

[19] J.A. Armstrong, N. Bloembergen, J. Ducuing, P.S. Pershan, Interactions between light waves in a nonlinear dielectric, Phys. Rev. 127 (6) (1962) 1918–1939, https://doi.org/10.1103/physrev.127.1918.

[20] Y.R. Shen, N. Bloembergen, Theory of stimulated Brillouin and Raman scattering, Phys. Rev. 137 (6A) (1965) A1787–A1805, https://doi.org/10.1103/physrev.137.a1787.
[21] C.-S. Wang, Theory of stimulated Raman scattering, Phys. Rev. 182 (2) (1969) 482–494, https://doi.org/10.1103/physrev.182.482.
[22] N. Bloembergen, Y.R. Shen, Coupling between vibrations and light waves in Raman laser media, Phys. Rev. Lett. 12 (18) (1964) 504–507, https://doi.org/10.1103/physrevlett.12.504.
[23] R.W. Hellwarth, Theory of stimulated Raman scattering, Phys. Rev. 130 (1963) 1850–1852, https://doi.org/10.1103/physrev.130.1850.
[24] N. Bloembergen, The stimulated Raman effect, Am. J. Phys. 35 (11) (1967) 989–1023, https://doi.org/10.1119/1.1973774.
[25] T. Yajima, M. Takatsuji, Higher order optical mixing of Raman laser light in nonlinear dielectric media, J. Phys. Soc. Jpn. 19 (12) (1964) 2343–2344, https://doi.org/10.1143/JPSJ.19.2343.
[26] P.D. Maker, R.W. Terhune, Study of optical effects due to an induced polarization third order in the electric field strength, Phys. Rev. 137 (1965) A801–A818.
[27] R.W. Minck, R.W. Terhune, W.G. Rado, Laser-stimulated Raman effect and resonant four-photon interactions in gases H_2, D_2, and CH_4, Appl. Phys. Lett. 3 (10) (1963) 181–184, https://doi.org/10.1063/1.1753840.
[28] G. Eckhardt, D.P. Bortfeld, M. Geller, Stimulated emission of Stokes and anti-Stokes Raman lines from diamond, calcite, and alpha-sulfur single crystals, Appl. Phys. Lett. 3 (8) (1963) 137–138, https://doi.org/10.1063/1.1753903.
[29] T.R. Loree, R.C. Sze, D.L. Barker, Efficient Raman shifting of ArF and KrF laser wavelengths, Appl. Phys. Lett. 31 (1) (1977) 37–39, https://doi.org/10.1063/1.89470.
[30] A.S. Eremenko, S.N. Karpukhin, A.I. Stepanov, Stimulated Raman scattering of the second harmonic of a neodymium laser in nitrate crystals, Sov. J. Quantum Electron, 10 (1) (1980) 113–114, https://doi.org/10.1070/qe1980v010n01abeh009872.
[31] A.M. Ivanchyuk, M.A. Terpogosyan, P.A. Shachverdov, V.D. Belayev, V.L. Ermolaev, N.P. Ticonova, SRS of the second harmonic of neodymium laser in nitrate crystals, Opt. Spectrosc. 59 (1985) 572–573.
[32] R.H. Stolen, E.P. Ippen, A.R. Tynes, Raman oscillation in glass optical waveguide, Appl. Phys. Lett. 20 (2) (1972) 62–64, https://doi.org/10.1063/1.1654046.
[33] K.X. Liu, E. Garmire, Understanding the formation of the SRS Stokes spectrum in fused silica fibers, IEEE J. Quantum Electron. 27 (4) (1991) 1022–1030, https://doi.org/10.1109/3.83337.
[34] K.O. Hill, B.S. Kawasaki, D.C. Johnson, Low-threshold CW Raman laser, Appl. Phys. Lett. 29 (3) (1976) 181–183, https://doi.org/10.1063/1.89016.
[35] C. Lin, R.H. Stolen, Backward Raman amplification and pulse steepening in silica fibers, Appl. Phys. Lett. 29 (7) (1976) 428–431, https://doi.org/10.1063/1.89107.
[36] J.C. Bouteiller, Raman fiber lasers for optical communication application, Ann. Télécommun. 58 (9–10) (2003) 1342–1363, https://doi.org/10.1007/bf03001734.
[37] L. Sirleto, M.A. Ferrara, Fiber amplifiers and fiber lasers based on stimulated Raman scattering: a review, Micromachines 11 (3) (2020) 247, https://doi.org/10.3390/mi11030247.
[38] J.A. Giordmaine, W. Kaiser, Light scattering by coherently driven lattice vibrations, Phys. Rev. 144 (2) (1965) 676–688, https://doi.org/10.1103/physrev.144.676.
[39] A. Laubereau, D. von der Linde, W. Kaiser, Decay time of hot to phonons in diamond, Phys. Rev. Lett. 27 (12) (1971) 802–805, https://doi.org/10.1103/physrevlett.27.802.
[40] R.R. Alfano, S.L. Shapiro, Optical phonon lifetime measured directly with picosecond pulses, Phys. Rev. Lett. 26 (20) (1971) 1247–1251, https://doi.org/10.1103/physrevlett.26.1247.
[41] A.J. DeMaria, W.H. Glenn Jr, M.J. Brienza, M.E. Mack, Picosecond laser pulses, Proc. IEEE 57 (1) (1969) 2–25, https://doi.org/10.1109/proc.1969.6864.
[42] E.B. Treacy, Compression of picosecond light pulses, Phys. Lett. A 28 (1) (1968) 34–35, https://doi.org/10.1016/0375-9601(68)90584-7.
[43] A. Laubereau, W. Kaiser, Vibrational dynamics of liquids and solids investigated by picosecond light pulses, Rev. Mod. Phys. 50 (3) (1978) 607–665, https://doi.org/10.1103/revmodphys.50.607.
[44] R.L. Fork, B.I. Greene, C.V. Shank, Generation of optical pulses shorter than 0.1 psec by colliding pulse mode locking, Appl. Phys. Lett. 38 (9) (1981) 671–672, https://doi.org/10.1063/1.92500.
[45] D. Strickland, G. Mourou, Compression of amplified chirped optical pulses, Opt. Commun. 55 (6) (1985) 447–449, https://doi.org/10.1016/0030-4018(85)90151-8.
[46] D.E. Spence, P.N. Kean, W. Sibbett, 60-fsec pulse generation from a self-mode-locked Ti:sapphire laser, Opt. Lett. 16 (1) (1991) 42, https://doi.org/10.1364/ol.16.000042.
[47] K.A. Nelson, R.J.D. Miller, D.R. Lutz, M.D. Fayer, Optical generation of tunable ultrasonic waves, J. Appl. Phys. 53 (2) (1982) 1144–1149, https://doi.org/10.1063/1.329864.
[48] M.M. Robinson, Y.-X. Yan, E.B. Gamble, L.R. Williams, J.S. Meth, K.A. Nelson, Picosecond impulsive stimulated Brillouin scattering: optical excitation of coherent transverse acoustic waves and application to time-domain investigations of structural phase transitions, Chem. Phys. Lett. 112 (6) (1984) 491–496, https://doi.org/10.1016/0009-2614(84)85764-4.
[49] S.D. Silvestri, J.G. Fujimoto, E.P. Ippen, E.B. Gamble, L.R. Williams, K.A. Nelson, Femtosecond time-resolved measurements of optic phonon dephasing by impulsive stimulated Raman scattering in α-perylene crystal from 20 to 300 K, Chem. Phys. Lett. 116 (2–3) (1985) 146–152, https://doi.org/10.1016/0009-2614(85)80143-3.
[50] S. Ruhman, A.G. Joly, K.A. Nelson, Time-resolved observations of coherent molecular vibrational motion and the general occurrence of impulsive stimulated scattering, J. Chem. Phys. 86 (11) (1987) 6563–6565, https://doi.org/10.1063/1.452400.

[51] L. Dhar, J.A. Rogers, K.A. Nelson, Time-resolved vibrational spectroscopy in the impulsive limit, Chem. Rev. 94 (1) (1994) 157–193, https://doi.org/10.1021/cr00025a006.
[52] J. Chesnoy, A. Mokhtari, Resonant impulsive-stimulated Raman scattering on malachite green, Phys. Rev. A 38 (7) (1988) 3566–3576, https://doi.org/10.1103/physreva.38.3566.
[53] S.L. Dexheimer, Q. Wang, L.A. Peteanu, W.T. Pollard, R.A. Mathies, C.V. Shank, Femtosecond impulsive excitation of nonstationary vibrational states in bacteriorhodopsin, Chem. Phys. Lett. 188 (1–2) (1992) 61–66, https://doi.org/10.1016/0009-2614(92)85089-s.
[54] T. Joo, A. Albrecht, Vibrational frequencies and dephasing times in excited electronic states by femtosecond time-resolved four-wave mixing, Chem. Phys. 173 (1) (1993) 17–26, https://doi.org/10.1016/0301-0104(93)80213-s.
[55] D.W. McCamant, P. Kukura, R.A. Mathies, Femtosecond time-resolved stimulated Raman spectroscopy: application to the ultrafast internal conversion in β-carotene, J. Phys. Chem. A 107 (40) (2003) 8208–8214, https://doi.org/10.1021/jp030147n.
[56] P. Kukura, D.W. McCamant, R.A. Mathies, Femtosecond stimulated Raman spectroscopy, Ann. Rev. Phys. Chem. 58 (2007) 461–488, https://doi.org/10.1146/annurev.physchem.58.032806.104456.
[57] N.A. Smith, S.R. Meech, Optically-heterodyne-detected optical Kerr effect (OHD-OKE): applications in condensed phase dynamics, Int. Rev. Phys. Chem. 21 (1) (2002) 75–100, https://doi.org/10.1080/01442350110092701.
[58] D. Heiman, R.W. Hellwarth, M.D. Levenson, G. Martin, Raman-induced Kerr effect, Phys. Rev. Lett. 36 (1976) 189–192, https://doi.org/10.1103/PhysRevLett.36.189.
[59] E. Ploetz, S. Laimgruber, S. Berner, W. Zinth, P. Gilch, Femtosecond stimulated Raman microscopy, Appl. Phys. B 87 (3) (2007) 389–393, https://doi.org/10.1007/s00340-007-2630-x.
[60] C.W. Freudiger, W. Min, B.G. Saar, S. Lu, G.R. Holtom, C. He, J.C. Tsai, J.X. Kang, X.S. Xie, Label-free biomedical imaging with high sensitivity by stimulated Raman scattering microscopy, Science 322 (5909) (2008) 1857–1861, https://doi.org/10.1126/science.1165758.
[61] A. Zumbusch, G.R. Holtom, X.S. Xie, Three-dimensional vibrational imaging by coherent anti-Stokes Raman scattering, Phys. Rev. Lett. 82 (1999) 4142–4145, https://doi.org/10.1103/physrevlett.82.4142.
[62] C.L. Evans, X.S. Xie, Coherent anti-Stokes Raman scattering microscopy: chemical imaging for biology and medicine, Ann. Rev. Anal. Chem. 1 (1) (2008) 883–909, https://doi.org/10.1146/annurev.anchem.1.031207.112754.
[63] J.-X. Cheng, X.S. Xie, Coherent Raman Scattering Microscopy, CRC Press, Baton Rouge, 2013.
[64] A. Alfonso-García, R. Mittal, E.S. Lee, E.O. Potma, Biological imaging with coherent Raman scattering microscopy: a tutorial, J. Biomed. Opt. 19 (7) (2014) 071407, https://doi.org/10.1117/1.jbo.19.7.071407.
[65] Leica TCS CARS: first confocal system with CARS imaging, Wiley Analytical Science, 2012. Tech. Rep.
[66] E.O. Potma, W.P de Boeij, D.A. Wiersma, Femtosecond dynamics of intracellular water probed with nonlinear optical Kerr effect microspectroscopy, Biophys. J. 80 (6) (2001) 3019–3024, https://doi.org/10.1016/s0006-3495(01)76267-4.
[67] B. Levine, C. Bethea, Ultrahigh sensitivity stimulated Raman gain spectroscopy, IEEE J. Quantum Electron. 16 (1) (1980) 85–89, https://doi.org/10.1109/jqe.1980.1070342.
[68] H.J. Lee, W. Zhang, D. Zhang, Y. Yang, B. Liu, E.L. Barker, K.K. Buhman, L.V. Slipchenko, M. Dai, J.-X. Cheng, Assessing cholesterol storage in live cells and *C. elegans* by stimulated Raman scattering imaging of phenyl-diyne cholesterol, Sci. Rep. 5 (1) (2015) 7930, https://doi.org/10.1038/srep07930.
[69] L. Wei, Z. Chen, L. Shi, R. Long, A.V. Anzalone, L. Zhang, F. Hu, R. Yuste, V.W. Cornish, W. Min, Super-multiplex vibrational imaging, Nature 544 (7651) (2017) 465–470, https://doi.org/10.1038/nature22051.
[70] D.P. Strommen, K. Nakamoto, Resonance Raman spectroscopy, J. Chem. Educ. 54 (8) (1977) 474, https://doi.org/10.1021/ed054p474.
[71] S. Shim, C.M. Stuart, R.A. Mathies, Resonance Raman cross-sections and vibronic analysis of Rhodamine 6G from broadband stimulated Raman spectroscopy, ChemPhysChem 9 (5) (2008) 697–699, https://doi.org/10.1002/cphc.200700856.
[72] L. Shi, H. Xiong, Y. Shen, R. Long, L. Wei, W. Min, Electronic resonant stimulated Raman scattering micro-spectroscopy, J. Phys. Chem. B 122 (39) (2018) 9218–9224, https://doi.org/10.1021/acs.jpcb.8b07037.
[73] L. Wei, W. Min, Electronic preresonance stimulated Raman scattering microscopy, J. Phys. Chem. Lett. 9 (15) (2018) 4294–4301, https://doi.org/10.1021/acs.jpclett.8b00204.
[74] M. Moskovits, Surface-enhanced spectroscopy, Rev. Mod. Phys. 57 (1985) 783–826.
[75] C.L. Haynes, A.D. Mcfarland, R.P. Van Duyne, Surface-enhanced Raman spectroscopy, Anal. Chem. 77 (17) (2005) 338A–346A.
[76] X. Wang, S.-C. Huang, S. Hu, S. Yan, B. Ren, Fundamental understanding and applications of plasmon-enhanced Raman spectroscopy, Nat. Rev. Phys. 2 (5) (2020) 253–271, https://doi.org/10.1038/s42254-020-0171-y.
[77] B.F. Levine, C.V. Shank, J.P. Heritage, Surface vibrational spectroscopy using stimulated Raman scattering, IEEE J. Quantum Electron. 15 (1979) 1418–1432.
[78] J. Heritage, J. Bergman, A. Pinczuk, J. Worlock, Surface picosecond Raman gain spectroscopy of a cyanide monolayer on silver, Chem. Phys. Lett. 67 (2) (1979) 229–232.
[79] E.L. Keller, N.C. Brandt, A.A. Cassabaum, R.R. Frontiera, Ultrafast surface-enhanced Raman spectroscopy, Analyst 140 (15) (2015) 4922–4931,- https://doi.org/10.1039/c5an00869g.
[80] H.K. Wickramasinghe, M. Chaigneau, R. Yasukuni, G. Picardi, R. Ossikovski, Billion-fold increase in tip-enhanced Raman signal, ACS Nano 8 (4) (2014) 3421–3426, https://doi.org/10.1021/nn406263m.
[81] A. Diaspro, P. Bianchini, Optical nanoscopy, La Rivista del Nuovo Cimento 43 (8) (2020) 385–455, https://doi.org/10.1007/s40766-020-00008-1.

[82] S.W. Hell, J. Wichmann, Breaking the diffraction resolution limit by stimulated emission: stimulated-emission-depletion fluorescence microscopy, Opt. Lett. 19 (11) (1994) 780, https://doi.org/10.1364/ol.19.000780.
[83] L. Gong, H. Wang, Suppression of stimulated Raman scattering by an electromagnetically-induced-transparency-like scheme and its application for super-resolution microscopy, Phys. Rev. A 92 (2) (2015) 023828, https://doi.org/10.1103/physreva.92.023828.
[84] L. Gong, H. Wang, Breaking the diffraction limit by saturation in stimulated-Raman-scattering microscopy: a theoretical study, Phys. Rev. A 90 (1) (2014) 013818, https://doi.org/10.1103/physreva.90.013818.
[85] W.R. Silva, C.T. Graefe, R.R. Frontiera, Toward label-free super-resolution microscopy, ACS Photonics 3 (1) (2016) 79–86, https://doi.org/10.1021/acsphotonics.5b00467.
[86] C.T. Graefe, D. Punihaole, C.M. Harris, M.J. Lynch, R. Leighton, R.R. Frontiera, Far-field super-resolution vibrational spectroscopy, Anal. Chem. 91 (14) (2019) 8723–8731, https://doi.org/10.1021/acs.analchem.9b01731.
[87] L. Gong, W. Zheng, Y. Ma, Z. Huang, Saturated stimulated-Raman-scattering microscopy for far-field superresolution vibrational imaging, Phys. Rev. Appl. 11 (2019) 034041, https://doi.org/10.1103/PhysRevApplied.11.034041.
[88] Y. Bi, C. Yang, Y. Chen, Y. Chen, S. Yan, G. Yang, Y. Wu, G. Zhang, P. Wang, Near-resonance enhanced label-free stimulated Raman scattering microscopy with spatial resolution near 130 nm, Light Sci. Appl. 7 (2018) 81, https://doi.org/10.1038/s41377-018-0082-1.
[89] S. Mukamel, Principles of Nonlinear Optical Spectroscopy, first ed., Oxford University Press, 1995.
[90] C.-Y. Chung, J. Hsu, S. Mukamel, E.O. Potma, Controlling stimulated coherent spectroscopy and microscopy by a position-dependent phase, Phys. Rev. A 87 (3) (2013) 033833, https://doi.org/10.1103/physreva.87.033833.
[91] M. Yoshizawa, Y. Hattori, T. Kobayashi, Femtosecond time-resolved resonance Raman gain spectroscopy in polydiacetylene, Phys. Rev. B 49 (1994) 13259–13262, https://doi.org/10.1103/PhysRevB.49.13259.
[92] M. Yoshizawa, H. Aoki, H. Hashimoto, Vibrational relaxation of the $2A_g^-$ excited state in all-trans-β-carotene obtained by femtosecond time-resolved Raman spectroscopy, Phys. Rev. B 63 (2001) 180301, https://doi.org/10.1103/PhysRevB.63.180301.
[93] D.R. Dietze, R.A. Mathies, Femtosecond stimulated Raman spectroscopy, ChemPhysChem 17 (9) (2016) 1224–1251, https://doi.org/10.1002/cphc.201600104.
[94] D.W. McCamant, P. Kukura, S. Yoon, R.A. Mathies, Femtosecond broadband stimulated Raman spectroscopy: apparatus and methods, Rev. Sci. Instrum. 75 (11) (2004) 4971–4980, https://doi.org/10.1063/1.1807566.
[95] S. Mukamel, J.D. Biggs, Communication: Comment on the effective temporal and spectral resolution of impulsive stimulated Raman signals, J. Chem. Phys. 134 (16) (2011) 161101, https://doi.org/10.1063/1.3581889.
[96] Y.-C. Wu, B. Zhao, S.-Y. Lee, Time-dependent wave packet averaged vibrational frequencies from femtosecond stimulated Raman spectra, J. Chem. Phys. 144 (5) (2016) 054104, https://doi.org/10.1063/1.4941057.
[97] M. Marrocco, Vectorial descriptions of nonlinear Raman microscopy, J. Raman Spectrosc. 41 (8) (2010) 882–889, https://doi.org/10.1002/jrs.2672.
[98] J.-X. Cheng, A. Volkmer, X.S. Xie, Theoretical and experimental characterization of coherent anti-Stokes Raman scattering microscopy, J. Opt. Soc. Am. B 19 (6) (2002) 1363, https://doi.org/10.1364/josab.19.001363.
[99] B. Richards, E. Wolf, Electromagnetic diffraction in optical systems, II. Structure of the image field in an aplanatic system, Proc. R. Soc. Lond. A. Math. Phys. Sci. 253 (1274) (1959) 358–379, https://doi.org/10.1098/rspa.1959.0200.
[100] Y. Li, B. Shen, S. Li, Y. Zhao, J. Qu, L. Liu, Review of stimulated Raman scattering microscopy techniques and applications in the biosciences, Adv. Biol. 5 (1) (2021) 2000184, https://doi.org/10.1002/adbi.202000184.
[101] D. Polli, V. Kumar, C.M. Valensise, M. Marangoni, G. Cerullo, Broadband coherent Raman scattering microscopy, Laser Photonics Rev. 12 (9) (2018) 1800020, https://doi.org/10.1002/lpor.201800020.
[102] H. Xiong, N. Qian, Z. Zhao, L. Shi, Y. Miao, W. Min, Background-free imaging of chemical bonds by a simple and robust frequency-modulated stimulated Raman scattering microscopy, Opt. Express 28 (10) (2020) 15663, https://doi.org/10.1364/oe.391016.
[103] D. Fu, F.-K. Lu, X. Zhang, C. Freudiger, D.R. Pernik, G. Holtom, X.S. Xie, Quantitative chemical imaging with multiplex stimulated Raman scattering microscopy, J. Am. Chem. Soc. 134 (8) (2012) 3623–3626, https://doi.org/10.1021/ja210081h.
[104] J. Réhault, F. Crisafi, V. Kumar, G. Ciardi, M. Marangoni, G. Cerullo, D. Polli, Broadband stimulated Raman scattering with Fourier-transform detection, Opt. Express 23 (19) (2015) 25235–25246, https://doi.org/10.1364/OE.23.025235.
[105] F.-K. Lu, M. Ji, D. Fu, X. Ni, C.W. Freudiger, G. Holtom, X.S. Xie, Multicolor stimulated Raman scattering microscopy, Mol. Phys. 110 (15–16) (2012) 1927–1932.
[106] M.N. Slipchenko, R.A. Oglesbee, D. Zhang, W. Wu, J.-X. Cheng, Heterodyne detected nonlinear optical imaging in a lock-in free manner, J. Biophotonics 5 (10) (2012) 801–807, https://doi.org/10.1002/jbio.201200005.
[107] K. Seto, Y. Okuda, E. Tokunaga, T. Kobayashi, Development of a multiplex stimulated Raman microscope for spectral imaging through multi-channel lock-in detection, Rev. Sci. Instrum. 84 (8) (2013) 083705, https://doi.org/10.1063/1.4818670.
[108] B. Marx, L. Czerwinski, R. Light, M. Somekh, P. Gilch, Multichannel detectors for femtosecond stimulated Raman microscopy—ideal and real ones, J. Raman Spectrosc. 45 (7) (2014) 521–527, https://doi.org/10.1002/jrs.4528.
[109] A. Ragni, G. Sciortino, M. Sampietro, G. Ferrari, D. Polli, Multi-channel lock-in based differential front-end for broadband Raman spectroscopy, Integration 67 (2019) 44–49, https://doi.org/10.1016/j.vlsi.2019.03.001.
[110] C. Zhang, D. Zhang, J.-X. Cheng, Coherent Raman scattering microscopy in biology and medicine, Annu. Rev. Biomed. Eng. 17 (1) (2014) 1–31,- https://doi.org/10.1146/annurev-bioeng-071114-040554.
[111] W.J. Tipping, M. Lee, A. Serrels, V.G. Brunton, A.N. Hulme, Stimulated Raman scattering microscopy: an emerging tool for drug discovery, Chem. Soc. Rev. 45 (2016) 2075–2089, https://doi.org/10.1039/c5cs00693g.

[112] F. Hu, L. Shi, W. Min, Biological imaging of chemical bonds by stimulated Raman scattering microscopy, Nat. Methods 16 (9) (2019) 830–842,- https://doi.org/10.1038/s41592-019-0538-0.
[113] A.H. Hill, D. Fu, Cellular imaging using stimulated Raman scattering microscopy, Anal. Chem. 91 (15) (2019) 9333–9342, https://doi.org/10.1021/acs.analchem.9b02095.
[114] B.G. Saar, C.W. Freudiger, J. Reichman, C.M. Stanley, G.R. Holtom, X.S. Xie, Video-rate molecular imaging in vivo with stimulated Raman scattering, Science 330 (6009) (2010) 1368–1370, https://doi.org/10.1126/science.1197236.
[115] D. Zhang, P. Wang, M.N. Slipchenko, J.-X. Cheng, Fast vibrational imaging of single cells and tissues by stimulated Raman scattering microscopy, Acc. Chem. Res. 47 (8) (2014), https://doi.org/10.1021/ar400331q.
[116] J.L. Suhalim, J.C. Boik, B.J. Tromberg, E.O. Potma, The need for speed, J. Biophotonics 5 (2012), https://doi.org/10.1002/jbio.201200002.
[117] Y. Ozeki, K. Itoh, Stimulated Raman scattering microscopy for live-cell imaging with high contrast and high sensitivity, Laser Phys. 20 (5) (2010) 1114–1118, https://doi.org/10.1134/s1054660x10090318.
[118] A. Folick, W. Min, M.C. Wang, Label-free imaging of lipid dynamics using coherent anti-Stokes Raman scattering (CARS) and stimulated Raman scattering (SRS) microscopy, Curr. Opin. Genet. Dev. 21 (5) (2011) 585–590, https://doi.org/10.1016/j.gde.2011.09.003.
[119] D. Zhang, M.N. Slipchenko, J.-X. Cheng, Highly sensitive vibrational imaging by femtosecond pulse stimulated Raman loss, J. Phys. Chem. Lett. 2 (11) (2011) 1248–1253, https://doi.org/10.1021/jz200516n.
[120] C. Cao, D. Zhou, T. Chen, A.M. Streets, Y. Huang, Label-free digital quantification of lipid droplets in single cells by stimulated Raman microscopy on a microfluidic platform, Anal. Chem. 88 (9) (2016) 4931–4939, https://doi.org/10.1021/acs.analchem.6b00862.
[121] A. García, J. Paugh, M. Farid, S. Garg, J. Jester, E. Potma, A machine learning framework to analyze hyperspectral stimulated Raman scattering microscopy images of expressed human meibum, J. Raman Spectrosc. 48 (6) (2017) 803–812, https://doi.org/10.1002/jrs.5118.
[122] M. Sunder, N. Acharya, S. Nayak, N. Mazumder, Optical spectroscopy and microscopy techniques for assessment of neurological diseases, Appl. Spectrosc. Rev. (2020) 1–40, https://doi.org/10.1080/05704928.2020.1851237.
[123] D. Lee, J. Du, R. Yu, Y. Su, J.R. Heath, L. Wei, Visualizing subcellular enrichment of glycogen in live cancer cells by stimulated Raman scattering, Anal. Chem. 92 (19) (2020) 13182–13191, https://doi.org/10.1021/acs.analchem.0c02348.
[124] S.W. Kim, C.R. Rho, J. Kim, Y. Xie, R.C. Prince, K. Mustafa, E.O. Potma, D.J. Brown, J.V. Jester, Eicosapentaenoic acid (EPA) activates PPARγ signaling leading to cell cycle exit, lipid accumulation, and autophagy in human meibomian gland epithelial cells (hMGEC), Ocular Surface 18 (3) (2020) 427–437, https://doi.org/10.1016/j.jtos.2020.04.012.
[125] K.-C. Huang, J. Li, C. Zhang, Y. Tan, J.-X. Cheng, Multiplex stimulated Raman scattering imaging cytometry reveals lipid-rich protrusions in cancer cells under stress condition, iScience 23 (3) (2020) 100953, https://doi.org/10.1016/j.isci.2020.100953.
[126] C.-R. Hu, D. Zhang, M.N. Slipchenko, J.-X. Cheng, B. Hu, Label-free real-time imaging of myelination in the *Xenopus Laevis* tadpole by in vivo stimulated Raman scattering microscopy, J. Biomed. Opt. 19 (8) (2014) 086005, https://doi.org/10.1117/1.jbo.19.8.086005.
[127] F.-K. Lu, S. Basu, V. Igras, M.P. Hoang, M. Ji, D. Fu, G.R. Holtom, V.A. Neel, C.W. Freudiger, D.E. Fisher, X.S. Xie, Label-free DNA imaging in vivo with stimulated Raman scattering microscopy, Proc. Natl. Acad. Sci. 112 (37) (2015) 11624–11629, https://doi.org/10.1073/pnas.1515121112.
[128] X. Zhang, M.B.J. Roeffaers, S. Basu, J.R. Daniele, D. Fu, C.W. Freudiger, G.R. Holtom, X.S. Xie, Label-free live-cell imaging of nucleic acids using stimulated Raman scattering microscopy, ChemPhysChem 13 (4) (2012) 1054–1059, https://doi.org/10.1002/cphc.201100890.
[129] J. Hou, J. Williams, E.L. Botvinick, E.O. Potma, B.J. Tromberg, Visualization of breast cancer metabolism using multimodal nonlinear optical microscopy of cellular lipids and redox state, Cancer Res. 78 (10) (2018) 2503–2512, https://doi.org/10.1158/0008-5472.can-17-2618.
[130] L. Zhang, W. Min, Bioorthogonal chemical imaging of metabolic changes during epithelial-mesenchymal transition of cancer cells by stimulated Raman scattering microscopy, J. Biomed. Opt. 22 (10) (2017) 1, https://doi.org/10.1117/1.jbo.22.10.106010.
[131] R. Mittal, M. Balu, T. Krasieva, E.O. Potma, L. Elkeeb, C.B. Zachary, P. Wilder-Smith, Evaluation of stimulated Raman scattering microscopy for identifying squamous cell carcinoma in human skin, Lasers Surg. Med. 45 (8) (2013) 496–502, https://doi.org/10.1002/lsm.22168.
[132] M. Ji, D.A. Orringer, C.W. Freudiger, S. Ramkissoon, X. Liu, D. Lau, A.J. Golby, I. Norton, M. Hayashi, N.Y.R. Agar, G.S. Young, C. Spino, S. Santagata, S. Camelo-Piragua, K.L. Ligon, O. Sagher, X.S. Xie, Rapid, label-free detection of brain tumors with stimulated Raman scattering microscopy, Sci. Transl. Med. 5 (201) (2013) 201ra119, https://doi.org/10.1126/scitranslmed.3005954.
[133] K.S. Shin, A.T. Francis, A.H. Hill, M. Laohajaratsang, P.J. Cimino, C.S. Latimer, L.F. Gonzalez-Cuyar, L.N. Sekhar, G. Juric-Sekhar, D. Fu, Intraoperative assessment of skull base tumors using stimulated Raman scattering microscopy, Sci. Rep. 9 (1) (2019) 20392, https://doi.org/10.1038/s41598-019-56932-8.
[134] B. Sarri, R. Canonge, X. Audier, E. Simon, J. Wojak, F. Caillol, C. Cador, D. Marguet, F. Poizat, M. Giovannini, H. Rigneault, Fast stimulated Raman and second harmonic generation imaging for intraoperative gastro-intestinal cancer detection, Sci. Rep. 9 (1) (2019) 10052, https://doi.org/10.1038/s41598-019-46489-x.
[135] L.A. Austin, S. Osseiran, C.L. Evans, Raman technologies in cancer diagnostics, Analyst 141 (2) (2015) 476–503, https://doi.org/10.1039/c5an01786f.
[136] J.L. Suhalim, C.-Y. Chung, M.B. Lilledahl, R.S. Lim, M. Levi, B.J. Tromberg, E.O. Potma, Characterization of cholesterol crystals in atherosclerotic plaques using stimulated Raman scattering and second-harmonic generation microscopy, Biophys. J. 102 (8) (2012) 1988–1995, https://doi.org/10.1016/j.bpj.2012.03.016.
[137] J. Moger, N. Garrett, Imaging cortical vasculature with stimulated Raman scattering and two-photon photothermal lensing microscopy, J. Raman Spectrosc. (2012), https://doi.org/10.1002/jrs.3156.

[138] P. Wang, J. Li, P. Wang, C.-R. Hu, D. Zhang, M. Sturek, J.-X. Cheng, Label-free quantitative imaging of cholesterol in intact tissues by hyperspectral stimulated Raman scattering microscopy, Angew. Chem. Int. Ed. 52 (49) (2013) 13042–13046, https://doi.org/10.1002/anie.201306234.
[139] J.R. Paugh, A. Alfonso-Garcia, A.L. Nguyen, J.L. Suhalim, M. Farid, S. Garg, J. Tao, D.J. Brown, E.O. Potma, J.V. Jester, Characterization of expressed human meibum using hyperspectral stimulated Raman scattering microscopy, Ocul. Surf. 17 (2018) 151–159, https://doi.org/10.1016/j.jtos.2018.10.003.
[140] K. Miao, L. Wei, Live-cell imaging and quantification of PolyQ aggregates by stimulated Raman scattering of selective deuterium labeling, ACS Central Sci. 6 (4) (2020) 478–486, https://doi.org/10.1021/acscentsci.9b01196.
[141] L. Shi, A.A. Fung, A. Zhou, Advances in stimulated Raman scattering imaging for tissues and animals, Quant. Imaging Med. Surg. 11 (3) (2020) 1078101, https://doi.org/10.21037/qims-20-712.
[142] B. Figueroa, W. Fu, T. Nguyen, K. Shin, B. Manifold, F. Wise, D. Fu, Broadband hyperspectral stimulated Raman scattering microscopy with a parabolic fiber amplifier source, Biomed. Opt. Express 9 (12) (2018) 6116, https://doi.org/10.1364/boe.9.006116.
[143] M. Ji, M. Arbel, L. Zhang, C.W. Freudiger, S.S. Hou, D. Lin, X. Yang, B.J. Bacskai, X.S. Xie, Label-free imaging of amyloid plaques in Alzheimer's disease with stimulated Raman scattering microscopy, Sci. Adv. 4 (11) (2018) eaat7715, https://doi.org/10.1126/sciadv.aat7715.
[144] S. He, C. Ye, Q. Sun, C.K. Leung, J.Y. Qu, Label-free nonlinear optical imaging of mouse retina, Biomed. Opt. Express 6 (3) (2015) 1055, https://doi.org/10.1364/boe.6.001055.
[145] S. Satoh, Y. Otsuka, Y. Ozeki, K. Itoh, A. Hashiguchi, K. Yamazaki, H. Hashimoto, M. Sakamoto, Label-free visualization of acetaminophen-induced liver injury by high-speed stimulated Raman scattering spectral microscopy and multivariate image analysis, Pathol. Int. 64 (10) (2014) 518–526, https://doi.org/10.1111/pin.12206.
[146] Z. Wang, W. Zheng, S.C.-Y. Hsu, Z. Huang, Optical diagnosis and characterization of dental caries with polarization-resolved hyperspectral stimulated Raman scattering microscopy, Biomed. Opt. Express 7 (4) (2016) 1284–1293, https://doi.org/10.1364/boe.7.001284.
[147] B. Zhang, H. Xu, J. Chen, X. Zhu, Y. Xue, Y. Yang, J. Ao, Y. Hua, M. Ji, Highly specific and label-free histological identification of microcrystals in fresh human gout tissues with stimulated Raman scattering, Theranostics 11 (7) (2021) 3074–3088, https://doi.org/10.7150/thno.53755.
[148] L. Wei, F. Hu, Y. Shen, Z. Chen, Y. Yu, C.-C. Lin, M.C. Wang, W. Min, Live-cell imaging of alkyne-tagged small biomolecules by stimulated Raman scattering, Nat. Methods 11 (4) (2014), https://doi.org/10.1038/nmeth.2878.
[149] C. Zeng, F. Hu, R. Long, W. Min, A ratiometric Raman probe for live-cell imaging of hydrogen sulfide in mitochondria by stimulated Raman scattering, Analyst 143 (2018) 4844–4848, https://doi.org/10.1039/c8an00910d.
[150] L. Wei, F. Hu, Z. Chen, Y. Shen, L. Zhang, W. Min, Live-cell bioorthogonal chemical imaging: stimulated Raman scattering microscopy of vibrational probes, Acc. Chem. Res. 49 (8) (2016) 1494–1502, https://doi.org/10.1021/acs.accounts.6b00210.
[151] L. Shi, C. Zheng, Y. Shen, Z. Chen, E.S. Silveira, L. Zhang, M. Wei, C. Liu, C.D. Sena-Tomas, K. Targoff, W. Min, Optical imaging of metabolic dynamics in animals, Nat. Commun. 9 (1) (2018) 2995, https://doi.org/10.1038/s41467-018-05401-3.
[152] G.A. Matanfack, J. Rüger, C. Stiebing, M. Schmitt, J. Popp, Imaging the invisible—bioorthogonal Raman probes for imaging of cells and tissues, J. Biophotonics 13 (9) (2020) e202000129, https://doi.org/10.1002/jbio.202000129.
[153] B.M. Lucotte, C. Powell, J.R. Knutson, C.A. Combs, D. Malide, Z.-X. Yu, M. Knepper, K.D. Patel, A. Pielach, E. Johnson, L. Borysova, K.A. Dora, R.S. Balaban, Direct visualization of the arterial wall water permeability barrier using CARS microscopy, Proc. Natl. Acad. Sci. 114 (18) (2017) 4805–4810, https://doi.org/10.1073/pnas.1620008114.
[154] G.A. Matanfack, J. Rüger, C. Stiebing, M. Schmitt, J. Popp, Imaging the invisible—bioorthogonal Raman probes for imaging of cells and tissues, J. Biophotonics 13 (9) (2020) e202000129, https://doi.org/10.1002/jbio.202000129.
[155] G.R. Littlejohn, J.C. Mansfield, J.T. Christmas, E. Witterick, M.D. Fricker, M.R. Grant, N. Smirnoff, R.M. Everson, J. Moger, J. Love, An update: improvements in imaging perfluorocarbon-mounted plant leaves with implications for studies of plant pathology, physiology, development and cell biology, Front. Plant Sci. 5 (2014) 140, https://doi.org/10.3389/fpls.2014.00140.
[156] Q. Hu, L.-L. Tay, M. Noestheden, J.P. Pezacki, Mammalian cell surface imaging with nitrile-functionalized nanoprobes: biophysical characterization of aggregation and polarization anisotropy in SERS imaging, J. Am. Chem. Soc. 129 (1) (2007) 14–15, https://doi.org/10.1021/ja0670005.
[157] J.M. Crawford, C. Portmann, X. Zhang, M.B.J. Roeffaers, J. Clardy, Small molecule perimeter defense in entomopathogenic bacteria, Proc. Natl. Acad. Sci. 109 (27) (2012) 10821–10826, https://doi.org/10.1073/pnas.1201160109.
[158] A. Alfonso-García, S.G. Pfisterer, H. Riezman, E. Ikonen, E.O. Potma, D38-cholesterol as a Raman active probe for imaging intracellular cholesterol storage, J. Biomed. Opt. 21 (6) (2016) 061003, https://doi.org/10.1117/1.jbo.21.6.061003.
[159] J. Li, J.-X. Cheng, Direct visualization of de novo lipogenesis in single living cells, Sci. Rep. 4 (1) (2014) 6807, https://doi.org/10.1038/srep06807.
[160] F. Hu, L. Wei, C. Zheng, Y. Shen, W. Min, Live-cell vibrational imaging of choline metabolites by stimulated Raman scattering coupled with isotope-based metabolic labeling, Analyst 139 (10) (2014) 2312–2317, https://doi.org/10.1039/c3an02281a.
[161] Y. Shen, F. Xu, L. Wei, F. Hu, W. Min, Live-cell quantitative imaging of proteome degradation by stimulated Raman scattering, Angew. Chem. Int. Ed. 53 (22) (2014) 5596–5599, https://doi.org/10.1002/anie.201310725.
[162] L. Wei, Y. Yu, Y. Shen, M.C. Wang, W. Min, Vibrational imaging of newly synthesized proteins in live cells by stimulated Raman scattering microscopy, Proc. Natl. Acad. Sci. 110 (28) (2013) 11226–11231, https://doi.org/10.1073/pnas.1303768110.
[163] F. Hu, L. Wei, C. Zheng, Y. Shen, W. Min, Live-cell vibrational imaging of choline metabolites by stimulated Raman scattering coupled with isotope-based metabolic labeling, Analyst 139 (10) (2014) 2312–2317, https://doi.org/10.1039/c3an02281a.
[164] H.-J. van Manen, A. Lenferink, C. Otto, Noninvasive imaging of protein metabolic labeling in single human cells using stable isotopes and Raman microscopy, Anal. Chem. 80 (24) (2008) 9576–9582, https://doi.org/10.1021/ac801841y.

[165] H. Yamakoshi, K. Dodo, A. Palonpon, J. Ando, K. Fujita, S. Kawata, M. Sodeoka, Alkyne-tag Raman imaging for visualization of mobile small molecules in live cells, J. Am. Chem. Soc. 134 (51) (2012) 20681–20689, https://doi.org/10.1021/ja308529n.
[166] N.M. Sijtsema, J.J. Duindam, G.J. Puppels, C. Otto, J. Greve, Imaging with extrinsic Raman labels, Appl. Spectrosc. 50 (5) (1996) 545–551, https://doi.org/10.1366/0003702963905989.
[167] J. Ni, R.J. Lipert, G.B. Dawson, M.D. Porter, Immunoassay readout method using extrinsic Raman labels adsorbed on immunogold colloids, Anal. Chem. 71 (21) (1999) 4903–4908, https://doi.org/10.1021/ac990616a.
[168] K. Meister, J. Niesel, U. Schatzschneider, N. Metzler-Nolte, D.A. Schmidt, M. Havenith, Label-free imaging of metal-carbonyl complexes in live cells by Raman microspectroscopy, Angew. Chem. Int. Ed. 49 (19) (2010) 3310–3312, https://doi.org/10.1002/anie.201000097.
[169] K. Sepp, M. Lee, M.T.J. Bluntzer, G.V. Helgason, A.N. Hulme, V.G. Brunton, Utilizing stimulated Raman scattering microscopy to study intracellular distribution of label-free ponatinib in live cells, J. Med. Chem. 63 (5) (2019) 2028–2034, https://doi.org/10.1021/acs.jmedchem.9b01546.
[170] H. Li, Y. Cheng, H. Tang, Y. Bi, Y. Chen, G. Yang, S. Guo, S. Tian, J. Liao, X. Lv, S. Zeng, M. Zhu, C. Xu, J.-X. Cheng, P. Wang, Imaging chemical kinetics of radical polymerization with an ultrafast coherent Raman microscope, Adv. Sci. 7 (10) (2020) 1903644, https://doi.org/10.1002/advs.201903644.
[171] R. Prince, P. Fan, Y. Lu, T. Baldacchini, E.O. Potma, Visualizing TPP structures with coherent Raman scattering microscopy, in: T. Baldacchini (Ed.), Three-Dimensional Microfabrication Using Two-Photon Polymerization, William Andrew, 2020, pp. 229–249, https://doi.org/10.1016/b978-0-12-817827-0.00055-2.
[172] T. Lee, H. Mundoor, D.G. Gann, T.J. Callahan, I.I. Smalyukh, Imaging of director fields in liquid crystals using stimulated Raman scattering microscopy, Opt. Express 21 (10) (2013) 12129, https://doi.org/10.1364/oe.21.012129.
[173] J. Duboisset, P. Berto, P. Gasecka, F.-Z. Bioud, P. Ferrand, H. Rigneault, S. Brasselet, Molecular orientational order probed by coherent anti-Stokes Raman scattering (CARS) and stimulated Raman scattering (SRS) microscopy: a spectral comparative study, J. Phys. Chem. B 119 (7) (2015) 3242–3249, https://doi.org/10.1021/jp5113813.
[174] G. Fleury, M.B.J. Roeffaers, Resolving the acid site distribution in Zn-exchanged ZSM-5 with stimulated Raman scattering microscopy, Catalysts 10 (11) (2020) 1331, https://doi.org/10.3390/catal10111331.
[175] B.G. Saar, Y. Zeng, C.W. Freudiger, Y.-S. Liu, M.E. Himmel, X.S. Xie, S.-Y. Ding, Label-free, real-time monitoring of biomass processing with stimulated Raman scattering microscopy, Angew. Chem. 122 (32) (2010) 5608–5611, https://doi.org/10.1002/ange.201000900.
[176] J.C. Mansfield, G.R. Littlejohn, M.P. Seymour, R.J. Lind, S. Perfect, J. Moger, Label-free chemically specific imaging in planta with stimulated Raman scattering microscopy, Anal. Chem. 85 (10) (2013) 5055–5063, https://doi.org/10.1021/ac400266a.
[177] Y. Suzuki, Y. Wakisaka, O. Iwata, A. Nakashima, T. Ito, M. Hirose, R. Domon, M. Sugawara, N. Tsumura, H. Watarai, T. Shimobaba, K. Suzuki, K. Goda, Y. Ozeki, High-speed stimulated Raman scattering microscopy for studying the metabolic diversity of motile *Euglena gracilis*, in: K.K. Tsia, K. Goda (Eds.), High-Speed Biomedical Imaging and Spectroscopy: Toward Big Data Instrumentation and Management II, vol. 10076, International Society for Optics and Photonics, SPIE, 2017, pp. 1–6, https://doi.org/10.1117/12.2250455.
[178] W. Shen, C. Collings, M. Li, J. Markovicz, J. Ralph, S.D. Mansfield, S.-Y. Ding, Imaging changes in cell walls of engineered poplar by stimulated Raman scattering and atomic force microscopy, ACS Sustain. Chem. Eng. 7 (12) (2019) 10616–10622, https://doi.org/10.1021/acssuschemeng.9b01166.
[179] T. Iino, K. Hashimoto, T. Asai, K. Kuchitsu, Y. Ozeki, Multicolour chemical imaging of plant tissues with hyperspectral stimulated Raman scattering microscopy, Analyst (2020), https://doi.org/10.1039/d0an02181d.
[180] M.N. Slipchenko, H. Chen, D.R. Ely, Y. Jung, M.T. Carvajal, J.-X. Cheng, Vibrational imaging of tablets by epi-detected stimulated Raman scattering microscopy, Analyst 135 (10) (2010) 2613–2619, https://doi.org/10.1039/c0an00252f.
[181] B.G. Saar, L.R. Contreras-Rojas, X.S. Xie, R.H. Guy, Imaging drug delivery to skin with stimulated Raman scattering microscopy, Mol. Pharm. 8 (3) (2011) 969–975, https://doi.org/10.1021/mp200122w.
[182] B. Figueroa, T. Nguyen, S. Sotthivirat, W. Xu, T. Rhodes, M.S. Lamm, R.L. Smith, C.T. John, Y. Su, D. Fu, Detecting and quantifying microscale chemical reactions in pharmaceutical tablets by stimulated Raman scattering microscopy, Anal. Chem. (2019), https://doi.org/10.1021/acs.analchem.9b01269.
[183] B. Sarri, R. Canonge, X. Audier, V. Lavastre, G. Pénarier, J. Alie, H. Rigneault, Discriminating polymorph distributions in pharmaceutical tablets using stimulated Raman scattering microscopy, J. Raman Spectrosc. 50 (12) (2019) 1896–1904, https://doi.org/10.1002/jrs.5743.
[184] W.J. Tipping, M. Lee, A. Serrels, V.G. Brunton, A.N. Hulme, Imaging drug uptake by bioorthogonal stimulated Raman scattering microscopy, Chem. Sci. 8 (8) (2017) 5606–5615, https://doi.org/10.1039/c7sc01837a.
[185] N.L. Garrett, B. Singh, A. Jones, J. Moger, Imaging microscopic distribution of antifungal agents in dandruff treatments with stimulated Raman scattering microscopy, J. Biomed. Opt. 22 (6) (2017) 066003, https://doi.org/10.1117/1.jbo.22.6.066003.
[186] A.T. Francis, T.T. Nguyen, M.S. Lamm, R. Teller, S.P. Forster, W. Xu, T. Rhodes, R.L. Smith, J. Kuiper, Y. Su, D. Fu, In situ stimulated Raman scattering (SRS) microscopy study of the dissolution of sustained-release implant formulation, Mol. Pharm. 15 (12) (2018) 5793–5801, https://doi.org/10.1021/acs.molpharmaceut.8b00965.
[187] W.R. Silva, E.L. Keller, R.R. Frontiera, Determination of resonance Raman cross-sections for use in biological SERS sensing with femtosecond stimulated Raman spectroscopy, Anal. Chem. 86 (15) (2014) 7782–7787, https://doi.org/10.1021/ac501701h.
[188] H. Xiong, L. Shi, L. Wei, Y. Shen, R. Long, Z. Zhao, W. Min, Stimulated Raman excited fluorescence spectroscopy and imaging, Nat. Photonics 13 (2019) 412–417, https://doi.org/10.1038/s41566-019-0396-4.
[189] H. Xiong, W. Min, Combining the best of two worlds: stimulated Raman excited fluorescence, J. Chem. Phys. 153 (21) (2020) 210901, https://doi.org/10.1063/5.0030204.

[190] M. Fleischmann, P. Hendra, A.J. McQuillan, Raman spectra of pyridine adsorbed at a silver electrode, Chem. Phys. Lett. 26 (2) (1974) 163–166,- https://doi.org/10.1016/0009-2614(74)85388-1.
[191] D.L. Jeanmaire, R.P. Van Duyne, Surface Raman spectroelectrochemistry: part I. Heterocyclic, aromatic, and aliphatic amines adsorbed on the anodized silver electrode, J. Electroanal. Chem. Interfacial Electrochem. 84 (1) (1977) 1–20, https://doi.org/10.1016/s0022-0728(77)80224-6.
[192] J. Wessel, Surface-enhanced optical microscopy, J. Opt. Soc. Am. B 2 (9) (1985) 1538–1541, https://doi.org/10.1364/JOSAB.2.001538.
[193] L. Novotny, N. van Hulst, Antennas for light, Nat. Photonics 5 (2011) 83–90.
[194] K. Kneipp, Y. Wang, H. Kneipp, L.T. Perelman, I. Itzkan, R.R. Dasari, M.S. Feld, Single molecule detection using surface-enhanced Raman scattering (SERS), Phys. Rev. Lett. 78 (1997) 1667–1670, https://doi.org/10.1103/PhysRevLett.78.1667.
[195] E.C. Le Ru, M. Meyer, P.G. Etchegoin, Proof of single-molecule sensitivity in surface enhanced Raman scattering (SERS) by means of a two-analyte technique, J. Phys. Chem. B 110 (4) (2006) 1944–1948, https://doi.org/10.1021/jp054732v.
[196] J.A. Dieringer, R.B. Lettan, K.A. Scheidt, R.P. Van Duyne, A frequency domain existence proof of single-molecule surface-enhanced Raman spectroscopy, J. Am. Chem. Soc. 129 (51) (2007) 16249–16256, https://doi.org/10.1021/ja077243c.
[197] C.K. Chen, A.R.B de Castro, Y.R. Shen, F. DeMartini, Surface coherent anti-Stokes Raman spectroscopy, Phys. Rev. Lett. 43 (1979) 946–949,- https://doi.org/10.1103/PhysRevLett.43.946.
[198] R.R. Frontiera, A.-I. Henry, N.L. Gruenke, R.P. Van Duyne, Surface-enhanced femtosecond stimulated Raman spectroscopy, J. Phys. Chem. Lett. 2 (10) (2011) 1199–1203, https://doi.org/10.1021/jz200498z.
[199] C. Zong, J.-X. Cheng, Origin of dispersive line shapes in plasmon-enhanced stimulated Raman scattering microscopy, Nanophotonics 10 (1) (2020) 617–625, https://doi.org/10.1515/nanoph-2020-0313.
[200] C. Zong, R. Premasiri, H. Lin, Y. Huang, C. Zhang, C. Yang, B. Ren, L.D. Ziegler, J.-X. Cheng, Plasmon-enhanced stimulated Raman scattering microscopy with single-molecule detection sensitivity, Nat. Commun. 10 (1) (2019) 5318, https://doi.org/10.1038/s41467-019-13230-1.
[201] F.T. Ladani, E.O. Potma, Dyadic Green's function formalism for photoinduced forces in tip-sample nanojunctions, Phys. Rev. B 95 (2017) 205440, https://doi.org/10.1103/PhysRevB.95.205440.
[202] I. Rajapaksa, H. Kumar Wickramasinghe, Raman spectroscopy and microscopy based on mechanical force detection, Appl. Phys. Lett. 99 (16) (2011) 161103, https://doi.org/10.1063/1.3652760.
[203] S. Li, S. Chen, J. Li, R. Wu, W. Ho, Joint space-time coherent vibration driven conformational transitions in a single molecule, Phys. Rev. Lett. 119 (2017) 176002, https://doi.org/10.1103/PhysRevLett.119.176002.

Further readings

R.C. Prince, R.R. Frontiera, E.O. Potma, Stimulated Raman scattering: from Bulk to Nano, Chem. Rev. 117 (7) (2017) 5070–5094, https://doi.org/10.1021/acs.chemrev.6b00545.

P. Kukura, D.W. McCamant, S. Yoon, D.B. Wandschneider, R.A. Mathies, Structural observation of the primary isomerization in vision with femtosecond-stimulated Raman, Science 310 (5750) (2005) 1006–1009, https://doi.org/10.1126/science.1118379.